Low-Speed Stability and Control Test of a "Double-Bubble" Transport Configuration

Dan D. Vicroy
Langley Research Center, Hampton, Virginia

NASA STI Program . . . in Profile

Since its founding, NASA has been dedicated to the advancement of aeronautics and space science. The NASA scientific and technical information (STI) program plays a key part in helping NASA maintain this important role.

The NASA STI program operates under the auspices of the Agency Chief Information Officer. It collects, organizes, provides for archiving, and disseminates NASA's STI. The NASA STI program provides access to the NTRS Registered and its public interface, the NASA Technical Reports Server, thus providing one of the largest collections of aeronautical and space science STI in the world. Results are published in both non-NASA channels and by NASA in the NASA STI Report Series, which includes the following report types:

- TECHNICAL PUBLICATION. Reports of completed research or a major significant phase of research that present the results of NASA Programs and include extensive data or theoretical analysis. Includes compilations of significant scientific and technical data and information deemed to be of continuing reference value. NASA counter-part of peer-reviewed formal professional papers but has less stringent limitations on manuscript length and extent of graphic presentations.

- TECHNICAL MEMORANDUM. Scientific and technical findings that are preliminary or of specialized interest, e.g., quick release reports, working papers, and bibliographies that contain minimal annotation. Does not contain extensive analysis.

- CONTRACTOR REPORT. Scientific and technical findings by NASA-sponsored contractors and grantees.

- CONFERENCE PUBLICATION. Collected papers from scientific and technical conferences, symposia, seminars, or other meetings sponsored or co-sponsored by NASA.

- SPECIAL PUBLICATION. Scientific, technical, or historical information from NASA programs, projects, and missions, often concerned with subjects having substantial public interest.

- TECHNICAL TRANSLATION. English-language translations of foreign scientific and technical material pertinent to NASA's mission.

Specialized services also include organizing and publishing research results, distributing specialized research announcements and feeds, providing information desk and personal search support, and enabling data exchange services.

For more information about the NASA STI program, see the following:

- Access the NASA STI program home page at http://www.sti.nasa.gov

- E-mail your question to help@sti.nasa.gov

- Phone the NASA STI Information Desk at 757-864-9658

- Write to:
  NASA STI Information Desk
  Mail Stop 148
  NASA Langley Research Center
  Hampton, VA 23681-2199

NASA/TM–2017-219797

Low-Speed Stability and Control Test of a "Double-Bubble" Transport Configuration

Dan D. Vicroy
Langley Research Center, Hampton, Virginia

December 2017

Abstract

A test in the Langley 12-Foot Low-Speed Tunnel was conducted as a risk mitigation effort to quickly obtain some low-speed stability and control data on a "double-bubble" or D8 transport configuration. The test also tested some configuration design trades. A 5-percent scale model was tested with stabilizer, elevator, rudder and aileron control deflections. This report summarizes the test results.

Introduction

The NASA Environmentally Responsible Aviation Project sponsored the development of advanced transport concepts that could meet a set of stretch goals to simultaneously reduced emissions, noise, field length and fuel burn, using projected 2030-2035 technologies. One of these advanced concepts was developed by a team from the Massachusetts Institute of Technology (MIT), Aurora Flight Sciences, Aerodyne Research and Pratt & Whitney [ref. 1]. This configuration featured a unique tandem tube fuselage cross section with aft-mounted turbo-fan engines imbedded in boundary-layer ingesting inlets. An artist's illustration of the concept is shown in figure 1. This concept was nicknamed the "double-bubble" or D8 due to its unique figure-eight cross section shape. Other unique configuration features are the stabilizer mounted on top of the twin vertical fins, called the Pi-tail, and the upward sloped nose section which is designed to minimize the cruise trim drag.

Figure 1 – Illustration of D8 advanced transport concept.

A series of refinement studies and wind tunnel tests over the past 4 years have progressed the design [refs 2-7]. The majority of these studies have focused on quantifying the potential benefit of the aft-mounted engines with the boundary layer ingesting inlets and the structural arrangement of the double-bubble fuselage. There has been limited focus on the stability and control aspects of the configuration. The D8 configuration is currently one of five configurations under consideration by the NASA New Aviation Horizons initiative for further development as a large-scale X-plane demonstrator. A test in the Langley 12-Foot Low-Speed Tunnel was proposed as a risk mitigation effort to quickly obtain some low-speed stability and control data and assess some configuration design trades. The outer mold lines and control surface definitions of an updated D8 configuration were provided to NASA by Aurora Flight Sciences on

May 9, 2016. Within 3 months the model was designed and fabricated, and testing began on August 11, 2016.

The objectives of the test were:

- Investigate the aerodynamics of the current D8 configuration at the edges of the flight envelope.

- Investigate the low-speed longitudinal and lateral/directional control characteristics of the configuration.

- Investigate the aerodynamic effects of nose and empennage configuration changes.

Nomenclature
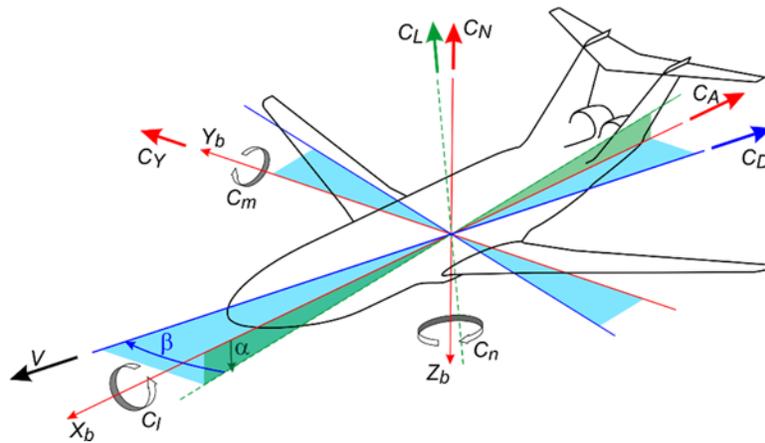
Figure 2 – Illustration of axes and force and moment orientations.

Symbols

b = reference span, ft

C_A = axial force coefficient, $\frac{\text{Axial force}}{\bar{q}S}$

C_D = drag force coefficient, $\frac{\text{Drag force}}{\bar{q}S}$

C_L = lift force coefficient, $\frac{\text{Lift force}}{\bar{q}S}$

C_l = rolling moment coefficient, $\frac{\text{Rolling moment}}{\bar{q}Sb}$

C_{l_β} = $\partial C_l / \partial \beta$, 1/radian

C_m = pitching moment coefficient, $\frac{\text{Pitching moment}}{\bar{q}S\bar{c}}$

C_N = normal force coefficient, $\frac{\text{Normal force}}{\bar{q}S}$

C_n = yawing moment coefficient, $\frac{\text{Yawing moment}}{\bar{q}Sb}$

C_{n_β} = $\partial C_n / \partial \beta$, 1/radian

C_Y = side force coefficient, $\frac{\text{Side force}}{\bar{q}S}$

C_{Y_β} = $\partial C_Y/\partial \beta$, 1/radian
$\bar{c}$ =   mean aerodynamic chord, ft
$\bar{q}$ =   free-stream dynamic pressure, lb/ft^2
Re =   Reynolds number
S =   reference area, ft^2
V =   velocity, ft/sec.
X_b, Y_b, Z_b =   body axes
x_{ac} =   horizontal coordinate of aerodynamic center, ft
x_{mrc} =   horizontal coordinate of moment reference center, ft
$\bar{x}_e$ =   elevator nondimensional horizontal moment arm
$\bar{x}_r$ =   rudder nondimensional horizontal moment arm
$\bar{x}_s$ =   stabilizer nondimensional horizontal moment arm
z_{ac} =   vertical coordinate of aerodynamic center, ft
z_{mrc} =   vertical coordinate of moment reference center, ft
$\bar{z}_s$ =   stabilizer nondimensional vertical moment arm
α =   angle of attack, deg.
β =   angle of sideslip, deg.
Δ =   difference or increment
δ_a =   aileron deflection, deg.
δ_e =   elevator deflection, deg.
δ_s =   stabilizer deflection, deg.
δ_r =   rudder deflection, deg.
σ =   standard deviation

Subscripts

a =   *aileron*
ac =   aerodynamic center
avg =   average
e =   elevator
mrc =   moment reference center
r =   rudder
s =   stabilizer

Abbreviations

LaRC   =   Langley Research Center
NASA   =   National Aeronautics and Space Administration

Test Setup

Model Description

The wind tunnel model was a 5-percent geometrically scaled version of a twin engine D8 transport configuration developed by Aurora Flight Sciences and MIT. A three-view drawing of the model is shown in figure 3. The model was primarily constructed with polycarbonate 3-D printed components mounted to an aluminum sub-structure frame. The model parts included aileron, stabilizer, elevator and rudder control surface deflections as well as two alternate empennage configurations and one alternate nose configuration. A list of the deflections produced for each control surface is provided in Table 1. Figure 4 shows a picture of the model with all the additional test parts.

$S = 3.127 \text{ ft}^2$
$\bar{c} = 0.62 \text{ ft}$
$b = 5.88 \text{ ft}$
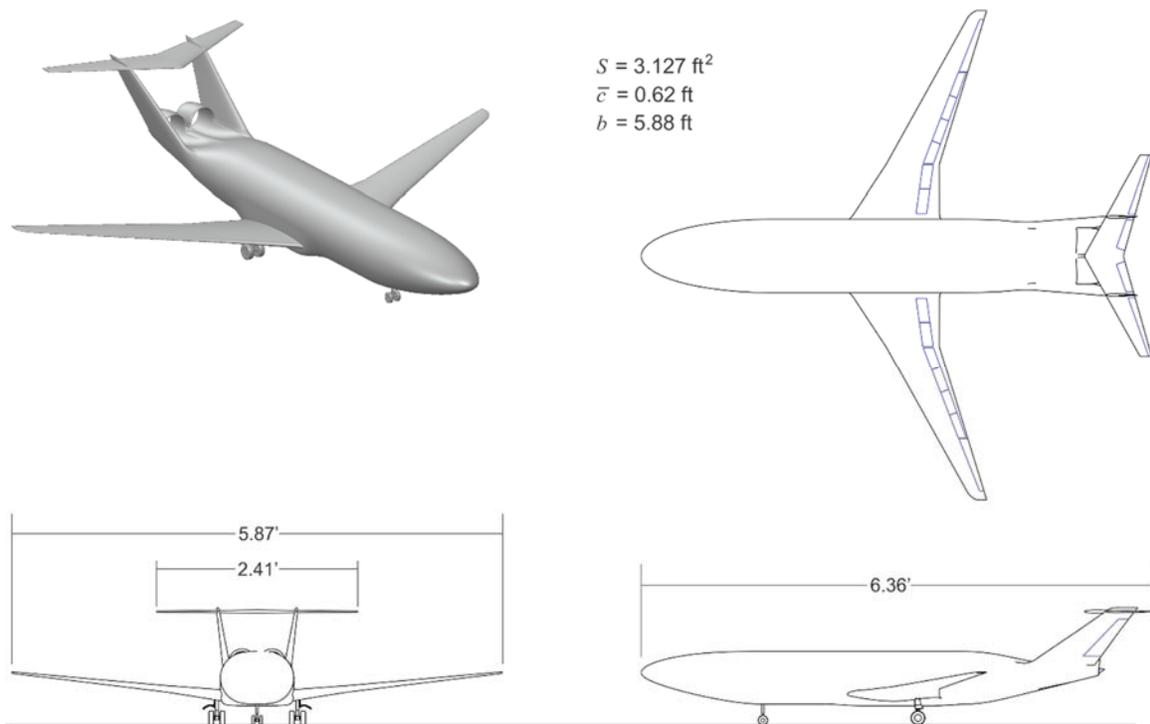
Figure 3 – Three-view drawing of 5-percent scale D8 model.

Table 1. Model control surface deflections.

Control surface	Deflection angles, deg.	Sign convention
Pi-tail stabilizer	-15, -10, -5, 0, 5	+ trailing edge down
Elevator	-25, -20, -15, -10, -5, 0, 5, 10, 15, 20, 25	+ trailing edge down
Right rudder	-25, -20, -15, -10, -5, 0, 5, 10, 15, 20, 25	+ trailing edge left
Left rudder	-25, -20, -15, -10, -5, 0, 5, 10, 15, 20, 25	+ trailing edge left
Right aileron	-20, -15, -10, -5, 0, 5, 10, 15, 20	+ trailing edge down
Left aileron	-20, -15, -10, -5, 0, 5, 10, 15, 20	+ trailing edge down

Figure 4 – Five-percent scale D8 model with configuration and control surface parts.

As noted in the introduction the baseline configuration has a unique upward sloped nose designed to reduce the cruise trim drag. This nose shape however introduces some cockpit window and pilot visibility challenges. An alternate, more conventional nose shape was produced to quantify the difference. A side-view comparison of the nose shapes is shown in figure 5.
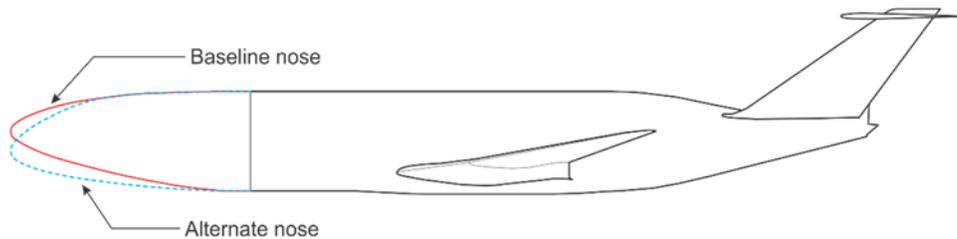

Figure 5 – Nose shape comparison.

In addition to the baseline Pi-tail empennage, two additional tail configurations were developed. One had a low horizontal stabilizer arrangement, designated the "Low-tail," and the other was an empennage without and any control surfaces or engine inlets, designated the "No-tail," as illustrated in figure 6.
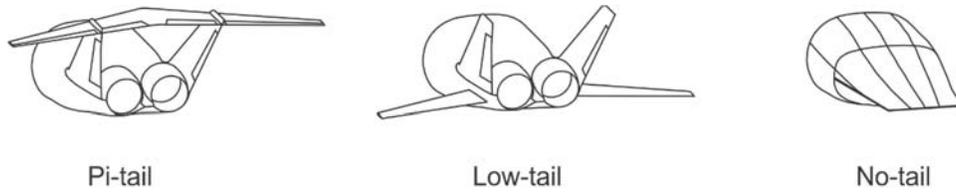
Figure 6 – Empennage configurations.

The original Pi-tail had a fixed horizontal stabilizer with 0 degrees of incidence. It was later decided to modify the Pi-tail to provide the additional stabilizer settings listed in Table 1. The tail was modified by cutting the vertical fins at the top of the rudder and fabricating new deflected stabilizer parts that included the vertical fin tips. This modified Pi-tail is designated as "Mod Pi-tail."

NASA Langley 12-Foot Low Speed Tunnel

The Langley 12-Foot Low Speed Tunnel began operations in 1939. The tunnel was originally designed and built to explore aircraft stability and control characteristics using a free-flight testing technique [refs. 8, 9]. The tunnel test section was designed to rotate about the pitch axis so as to match the flight path angle of a free-flying remote controlled model. The test section is enclosed in a sphere to allow for the air recirculation as the test section is rotated, as illustrated in figure 7. The octagonal test section has a height and width of 12 feet and a relatively short length of 15 feet. In the early 1950s the free-flight testing moved to the much larger 30- by 60-foot Full-Scale Tunnel the 12-Foot test section was horizontally fixed. It is now used for exploratory research and low-speed stability and control data.

The tunnel operates at atmospheric pressure with a maximum freestream dynamic pressure of 7 psf. It is driven by a 6-bladed, 15.8 foot diameter fan. For this test the bulk of the testing was at a dynamic pressure of 4 psf. All of the data presented in this report will be at 4 psf unless specifically noted otherwise.
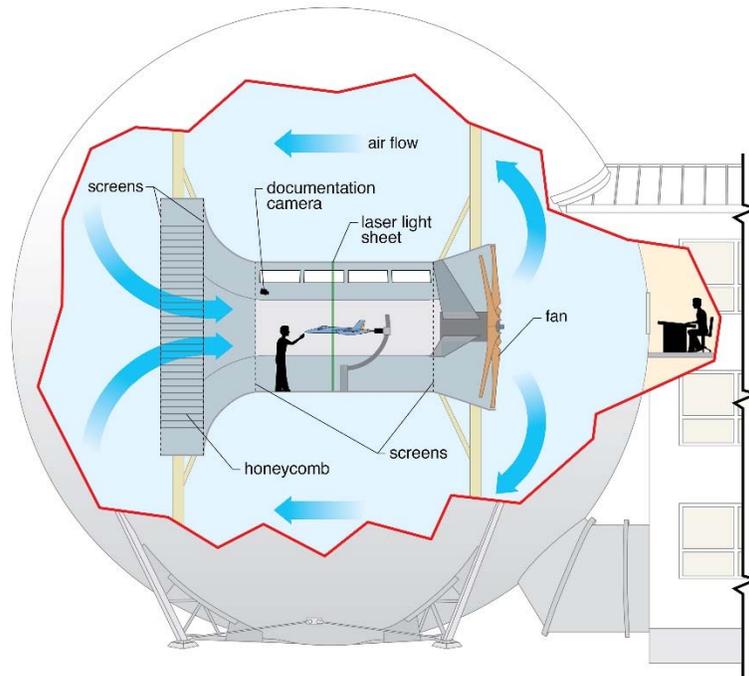
Figure 7 – Illustration of 12-Foot Low-Speed Tunnel.

The model with an internal strain gauge balance was mounted on a bent sting connected to the tunnel C-strut, as illustrated in figure 8. The C-strut provides a pitch angle range from -10 to 90 degrees and can be yawed ±90 degrees.
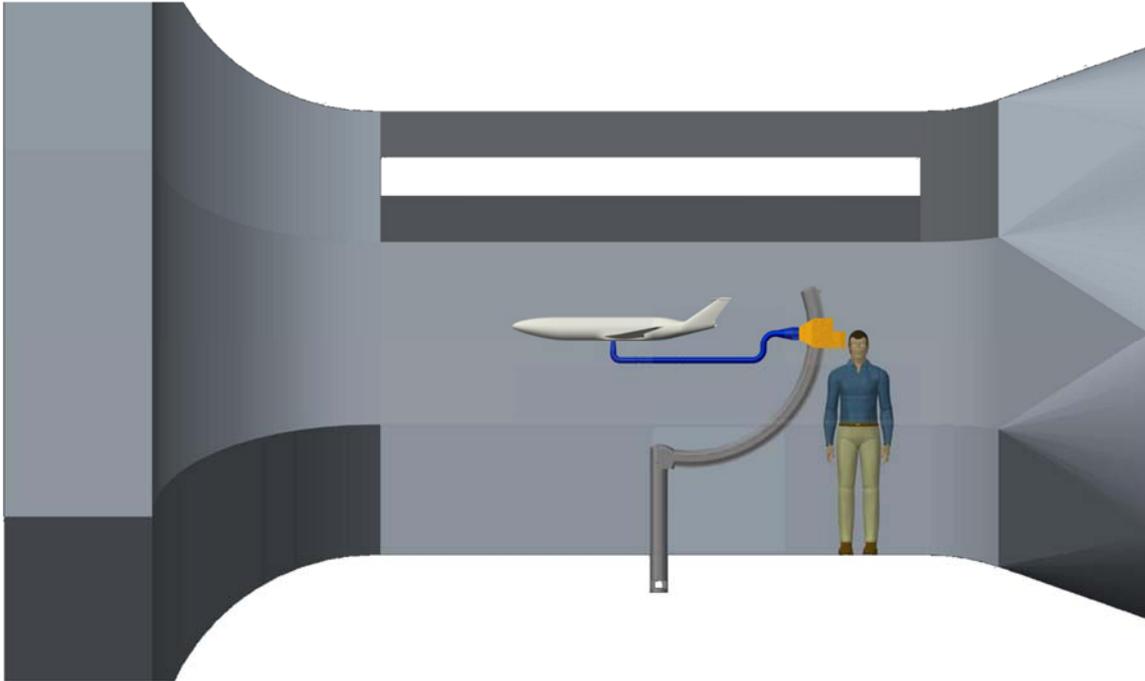

Figure 8 – Illustration of installation in 12-Foot Low-Speed Tunnel.

Instrumentation

Force and moment measurements were obtained with the Langley FF-09D internal, six-component, strain gauge balance. The maximum load range and calibration accuracy (95% confidence interval) of the balance are listed in Table 2.

Table 2. FF-09D strain gauge balance load capacities.

	Max load	**Accuracy % max**	**Accuracy units**
Normal Force	± 100.0 lb	0.04	0.04 lb
Pitching Moment	± 480.0 in-lb	0.04	0.192 in-lb
Side Force	± 60.0 lb	0.07	0.04 lb
Yawing Moment	± 540.0 in lb	0.03	0.162 in-lb
Rolling Moment	± 176.8 in lb	0.11	0.194 in-lb
Axial Force	± 50.0 lb	0.05	0.03 lb

The pitch and yaw angles of the model were measured from encoders on the tunnel C-strut system. Pre-test loading of the C-strut sting indicated less than 0.5 degrees of sting bending at the maximum normal balance load. No sting bending corrections were applied to the data.

Data Processing

The balance force and moment readings for each data point are sampled for 10 seconds at a sampling rate of 50 Hz. The measurements are filtered with a 1 Hz low-pass filter and then averaged over the 10 second sample interval.

No flow angularity or installation corrections were applied to the data.

Results and Discussion

As mentioned above in the facility description section, all of the data results presented are for a dynamic pressure ($\bar{q}$) of 4 psf unless specifically noted otherwise.

Data Repeatability

The force and moment coefficient repeatability values are presented in figures 9 and 10. The repeatability values were computed by collecting all the runs of repeated configurations (same nose, empennage and control deflections) and then computing the mean values for each repeated configuration at common angle of attack points. The difference from the mean values were computed for each run and plotted on the repeatability figure with a different symbol for each repeat configuration. The combined standard deviations of all the repeat configuration values were then computed for each common angle of attack value. Black dashed lines showing twice the standard deviation value are shown on the figure. Also shown are green solid lines indicating twice the standard deviation of the balance calibration for a test dynamic pressure of 4 psf.

Good repeatability results were obtained for the axial coefficient. All the other coefficient values had larger repeatability variations than the balance calibration accuracy. Figure 10 shows the repeatability for the wind axis lift and drag coefficients. The effect of the normal force variability on the drag repeatability is clearly evident with increased angle of attack.
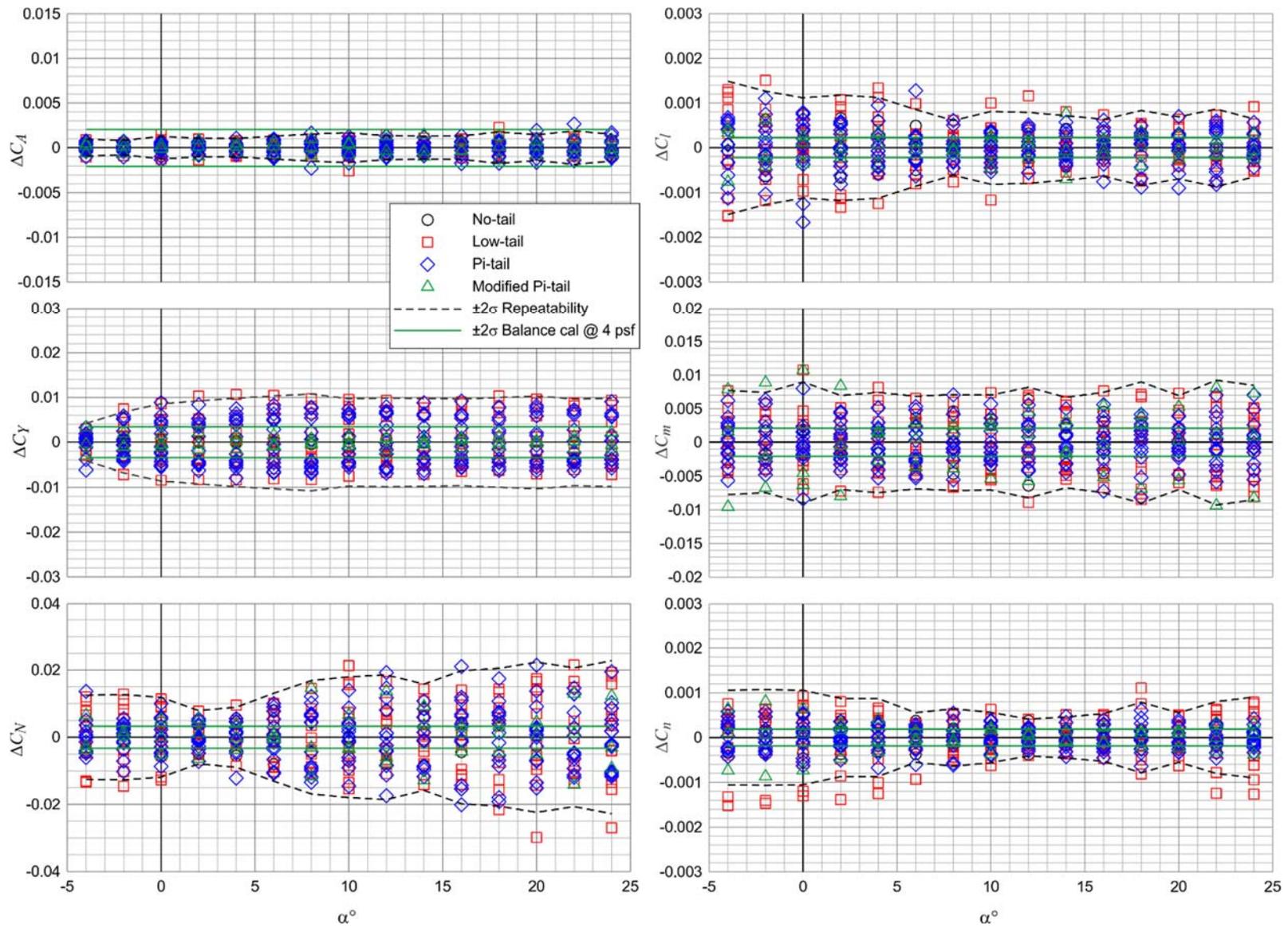
Figure 9 – Repeat data variation from the mean of common test configurations.

9
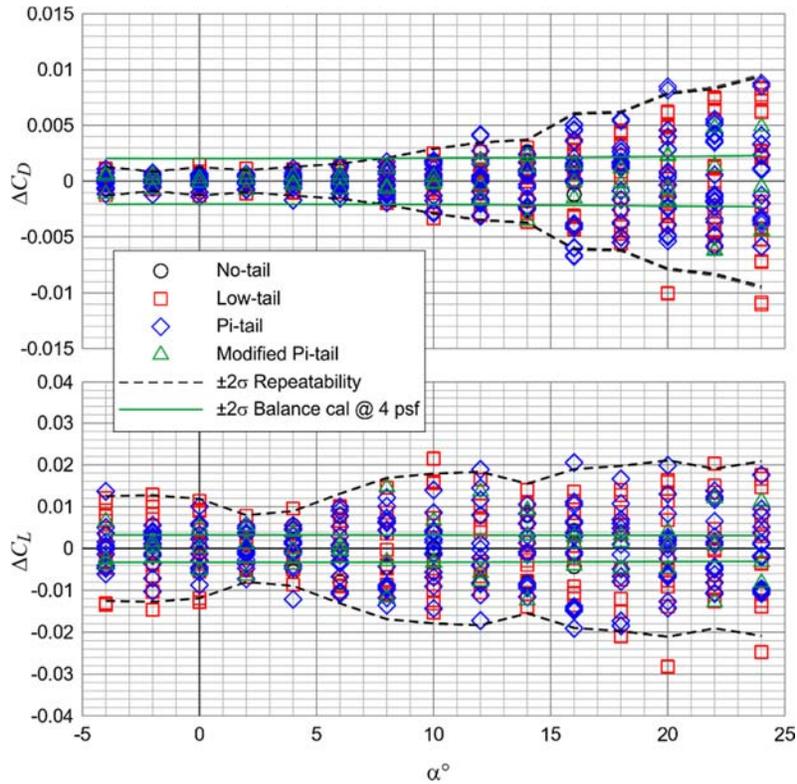
Figure 10 – Lift and drag coefficient repeat variation from the mean of common test configurations.

Configuration Aerodynamics

This section will review the basic aerodynamics of the three empennage configurations as well as the alternate nose shape.

Pi-tail Configuration

The Pi-tail empennage is the baseline configuration for this D8 model and is shown in figure 11 mounted in the tunnel. The effect of Reynolds number variation on the longitudinal coefficients is shown in figure 12 over the nominal angle of attack test range from -4 to 24 degrees. Increasing the Reynolds number over a limited range resulted in an incremental reduction in the pitching moment, an increase in the zero-angle-of-attack lift with a reduction in the lift curve slope, and a slight reduction in the minimum drag.
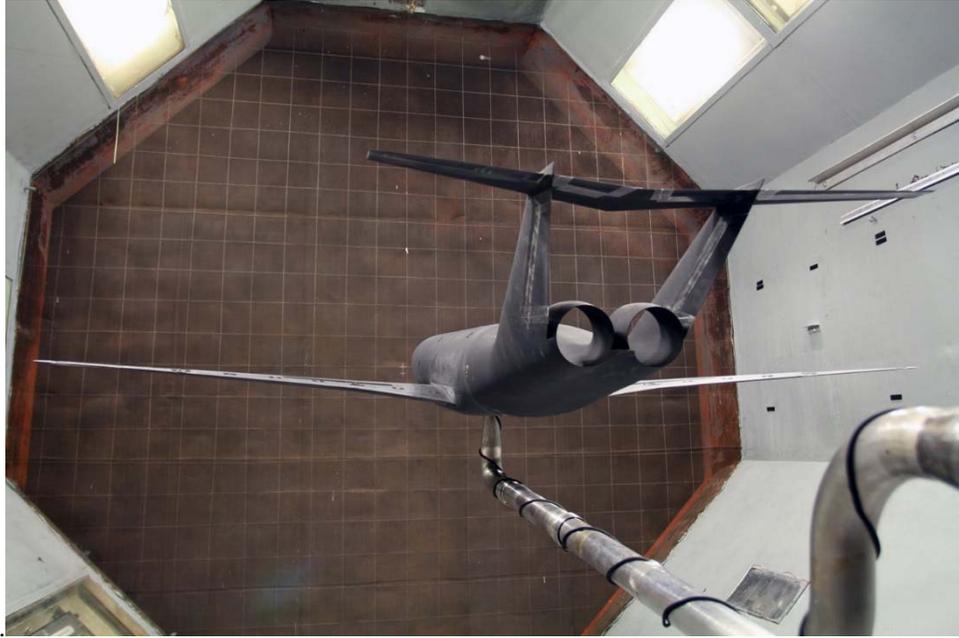
Figure 11 – Aft view of Pi-tail configuration in the tunnel.
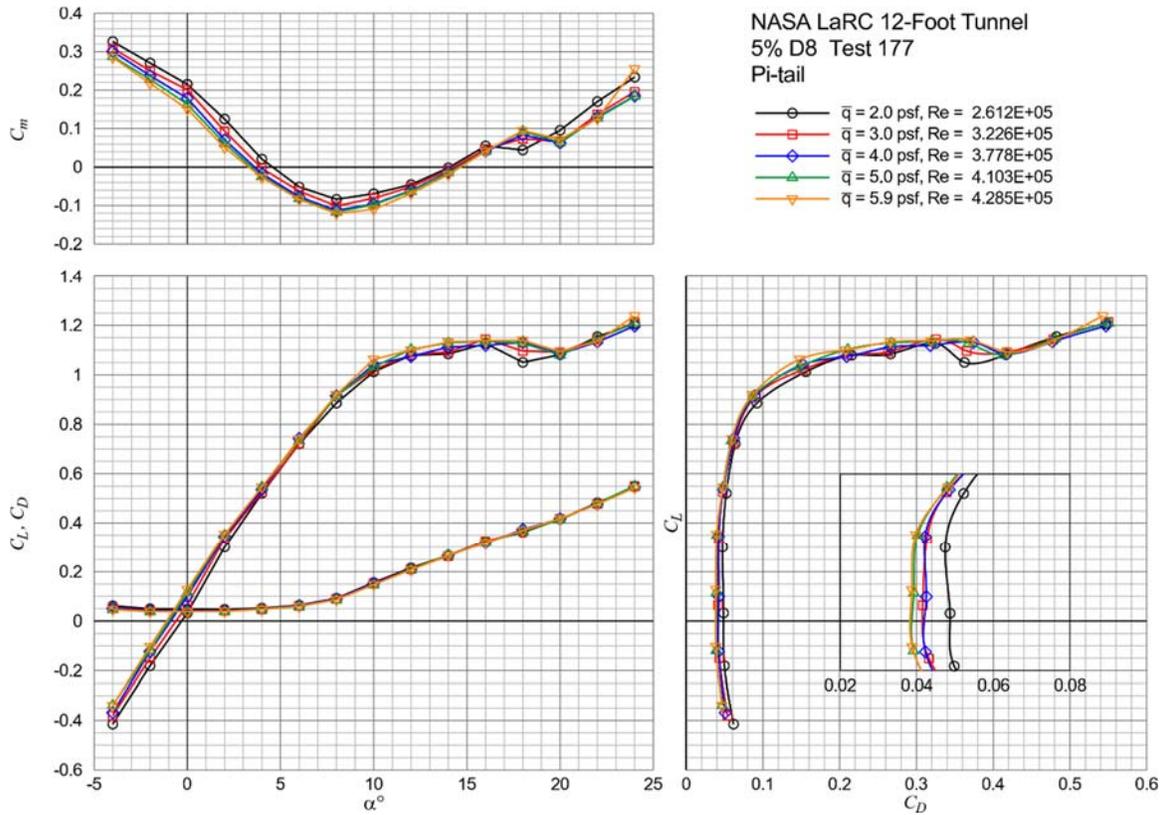
Figure 12 – Effect of Reynolds number on longitudinal coefficients of the baseline Pi-tail configuration.

The forces and moments of the baseline Pi-tail configuration over the nominal angle of attack and sideslip range are presented in figures 13 thru 16. Note the lift and drag coefficients are wind axis values, whereas the remaining coefficients are relative to the body axis, as previously illustrated in figure 2. The open symbols with the dashed lines are for negative sideslip values and the solid symbols with solid lines are for positive sideslip values. The effect of sideslip angle on the longitudinal coefficients is fairly symmetric with positive or negative sideslip values, as is expected for a symmetric model in uniform flow. The pitching moment decreases and the minimum drag and maximum lift increases with larger magnitudes of sideslip.

The effects of sideslip on the lateral/directional coefficients are presented in figures 14 thru 16. Figure 14 shows the coefficient values over the nominal angle of attack range at fixed sideslip values. The lateral/directional coefficient values should be zero for zero sideslip angle. The yawing moment and side force coefficients are nearly zero across the angle of attack range. However, the zero-sideslip rolling moment coefficient shows some non-zero variation which could be due to model asymmetry or non-uniform flow in the tunnel. Taking the difference between the non-zero-sideslip coefficient values and the zero-sideslip coefficient values provides a better indication of the effect of sideslip on the lateral/directional coefficients. These results are presented in figure 15. Presented in this manner the positive and negative sideslip results should overlay each other. The rolling moment and sideforce values do show good positive and negative agreement up thru about 14 degrees angle of attack. The yawing moment however showed more positive to negative variation. Figure 16 presents the same data values as figure 15 but shows the change in the coefficient values with sideslip variation at constant angle of attack values. The change in the lateral/directional coefficients is nearly linear with sideslip angle.
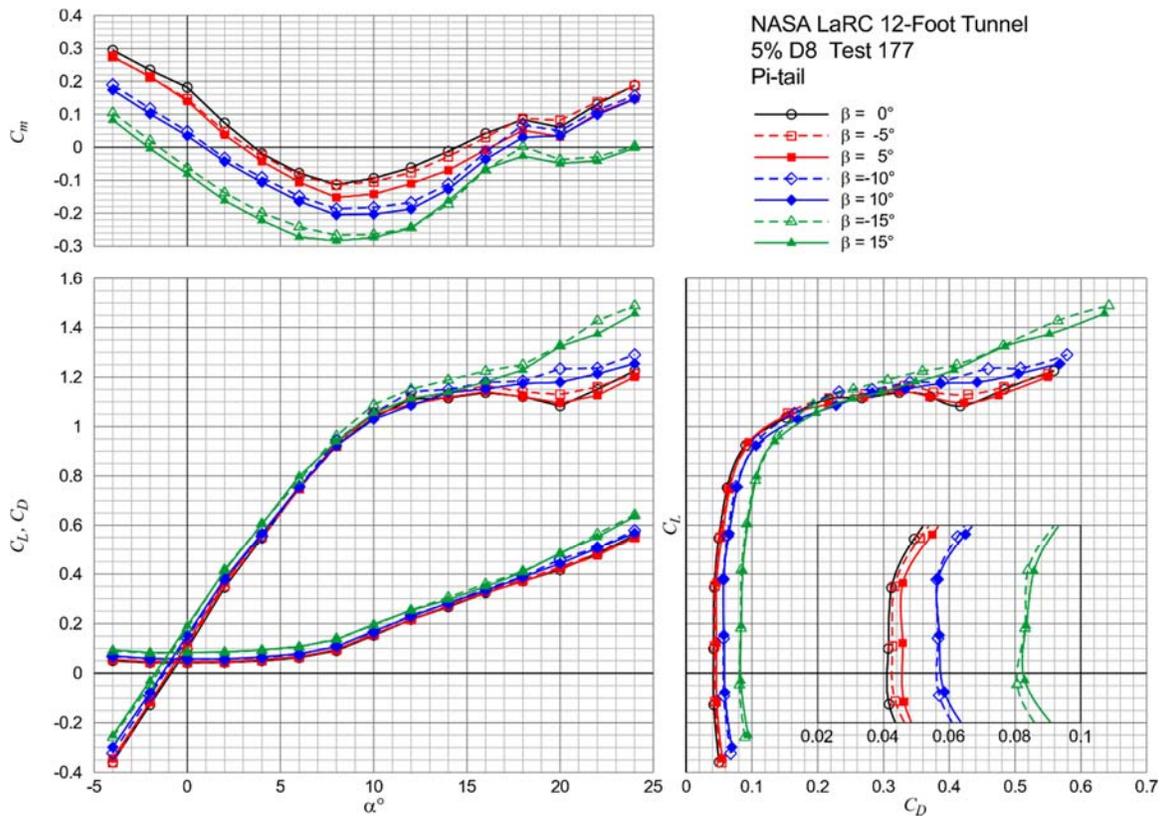
Figure 13 – Effect of sideslip angle on longitudinal coefficients of the baseline Pi-tail configuration.
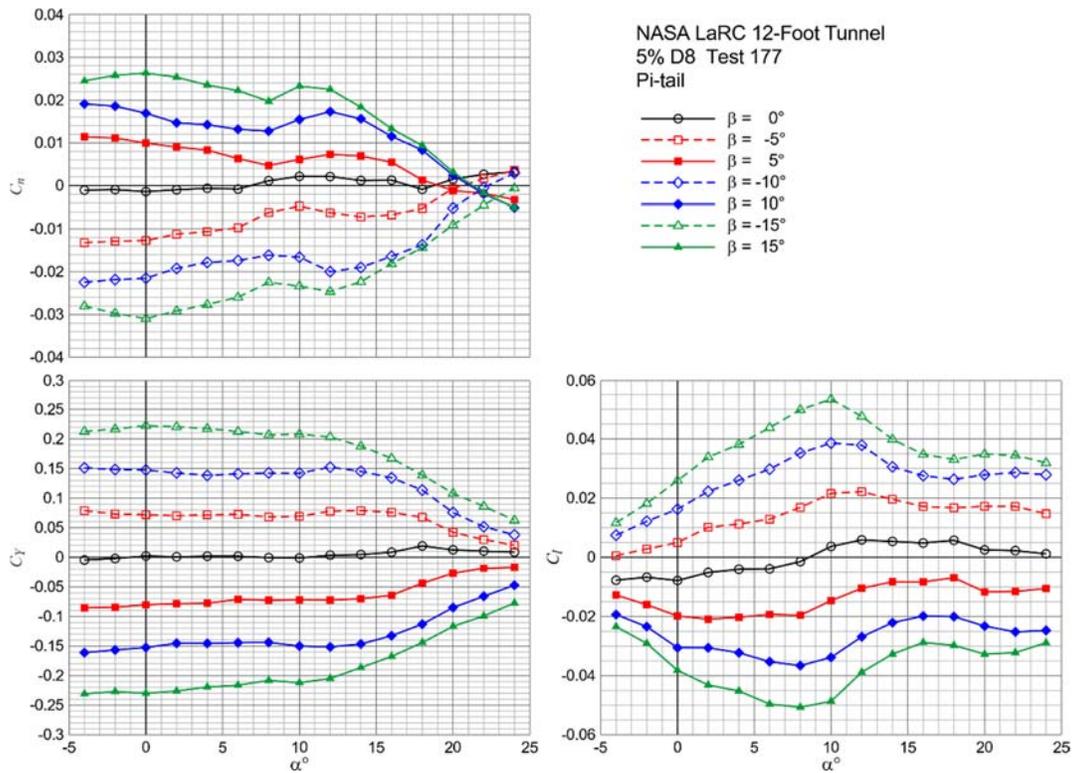
Figure 14 – Effect of sideslip angle on lateral/directional coefficients of the baseline Pi-tail configuration.
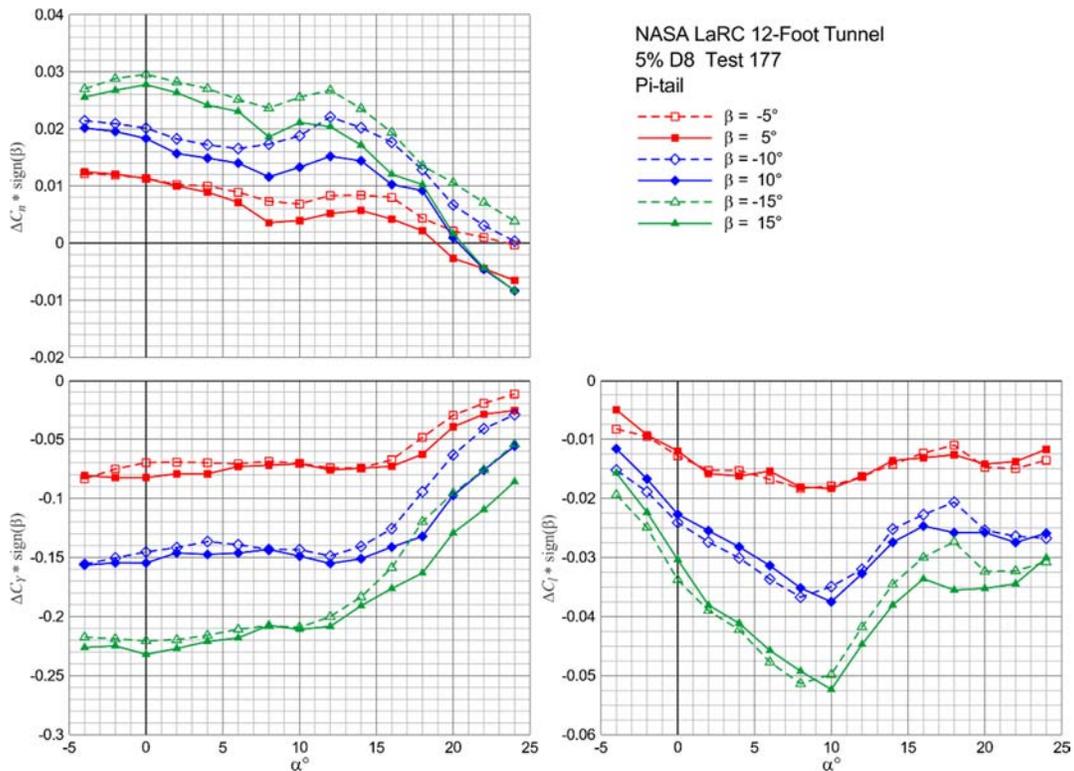

Figure 15 – Change in lateral/directional coefficients of the baseline Pi-tail configuration with angle of attack.
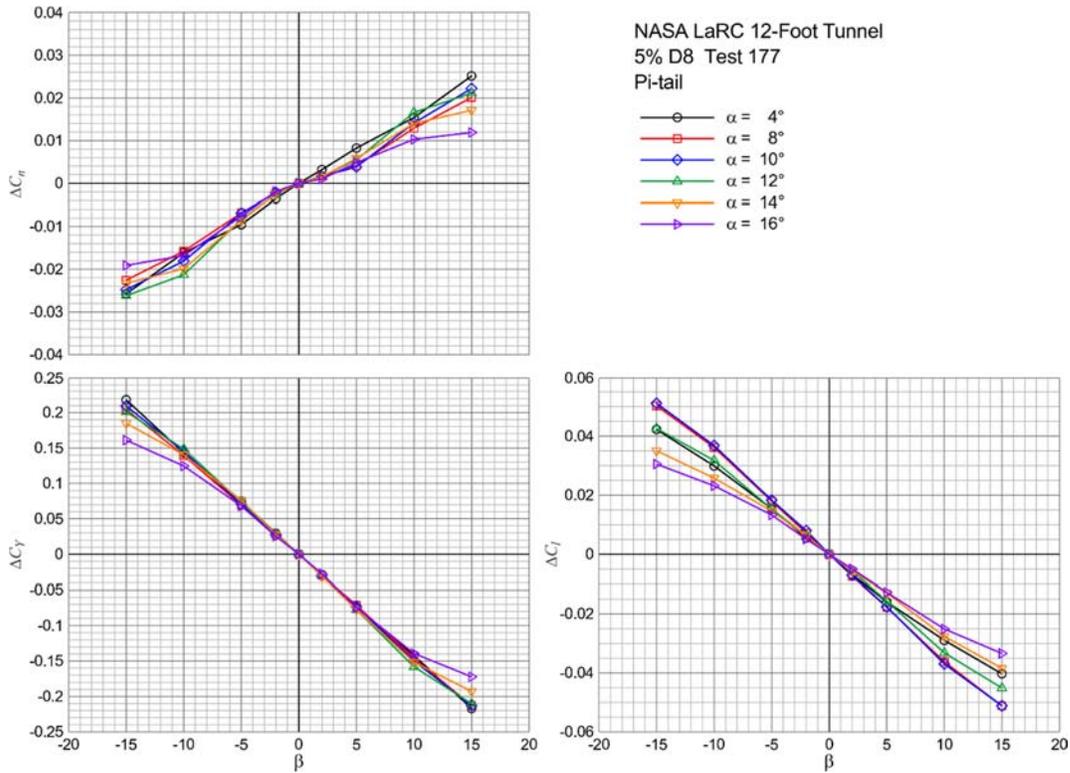
Figure 16 – Change in lateral/directional coefficients of the baseline Pi-tail configuration with sideslip angle.

Effect of Nose Shape

The unique upward sloped nose of the baseline configuration is designed to reduce the cruise trim drag. This nose shape however introduces some cockpit window and pilot visibility challenges. An alternate, more conventional nose shape was produced to quantify the difference. The effect of the nose shape on the longitudinal coefficients is shown in figure 17. There was no effective difference in the lift and drag coefficients. The primary effect was a nearly constant 0.03 pitching moment increment, with the baseline nose being the larger of the two, i.e., more nose-up.
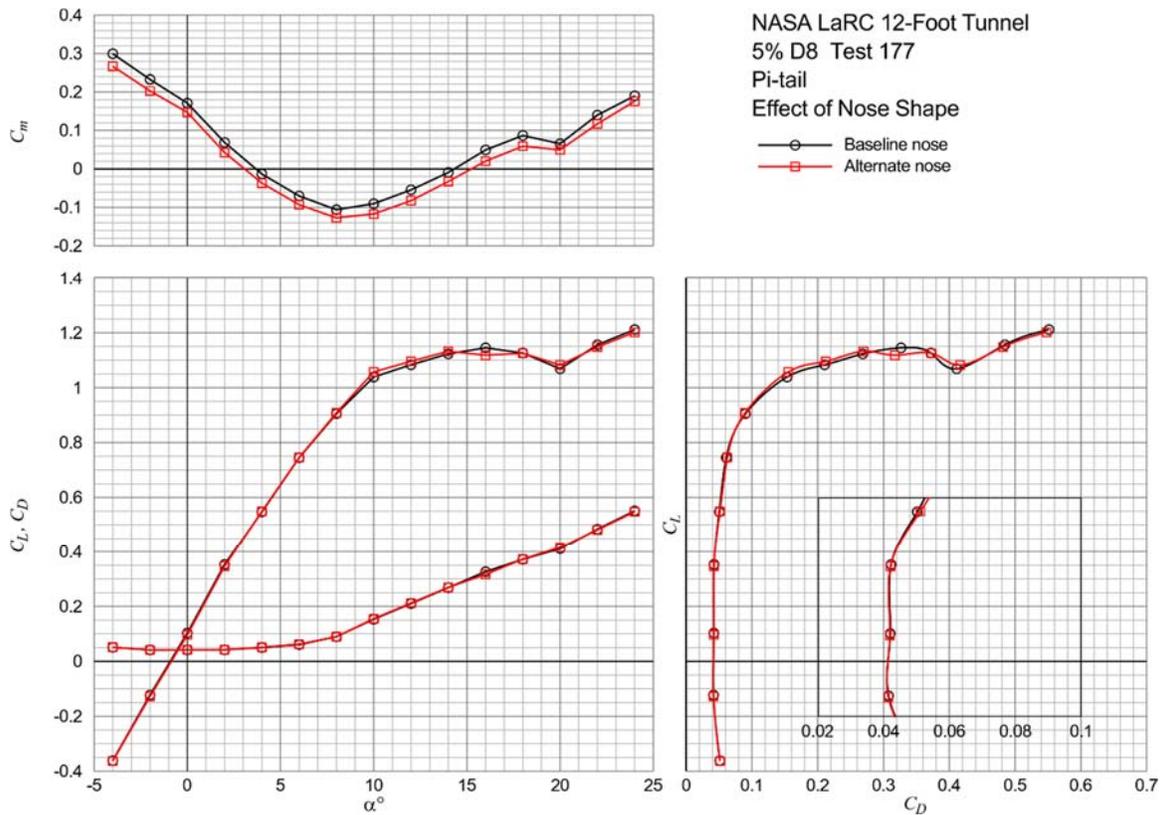
Figure 17 – Effect of nose shape on longitudinal coefficients of the Pi-tail configuration.

Low-tail Configuration

The Low-tail configuration is shown mounted in the tunnel in figure 18. The forces and moment coefficients of this configuration over the nominal angle of attack and sideslip range are presented in figures 19 thru 21. The effect of sideslip angle on the longitudinal coefficients has the same trends as the Pi-tail values shown in figure 13. The pitching moment decreases and the minimum drag and maximum lift both increase with larger magnitudes of sideslip.

The effects of sideslip on the lateral/directional coefficients are presented in figures 20 and 21. Figure 20 shows the coefficients values over the nominal angle of attack range at fixed sideslip values. Similar to the Pi-tail values shown in figure 15, the rolling moment and sideforce values show good positive and negative agreement up thru about 14 degrees angle of attack and the yawing moment had more positive to negative variation. The change in the lateral/directional coefficients with sideslip variation at constant angle of attack values are shown in figure 21. The Low-tail provided a slightly higher change in sideforce and yawing moment with sideslip angle than the Pi-tail results shown in figure 16.

Figure 18 – Aft view of Low-tail configuration in the tunnel.
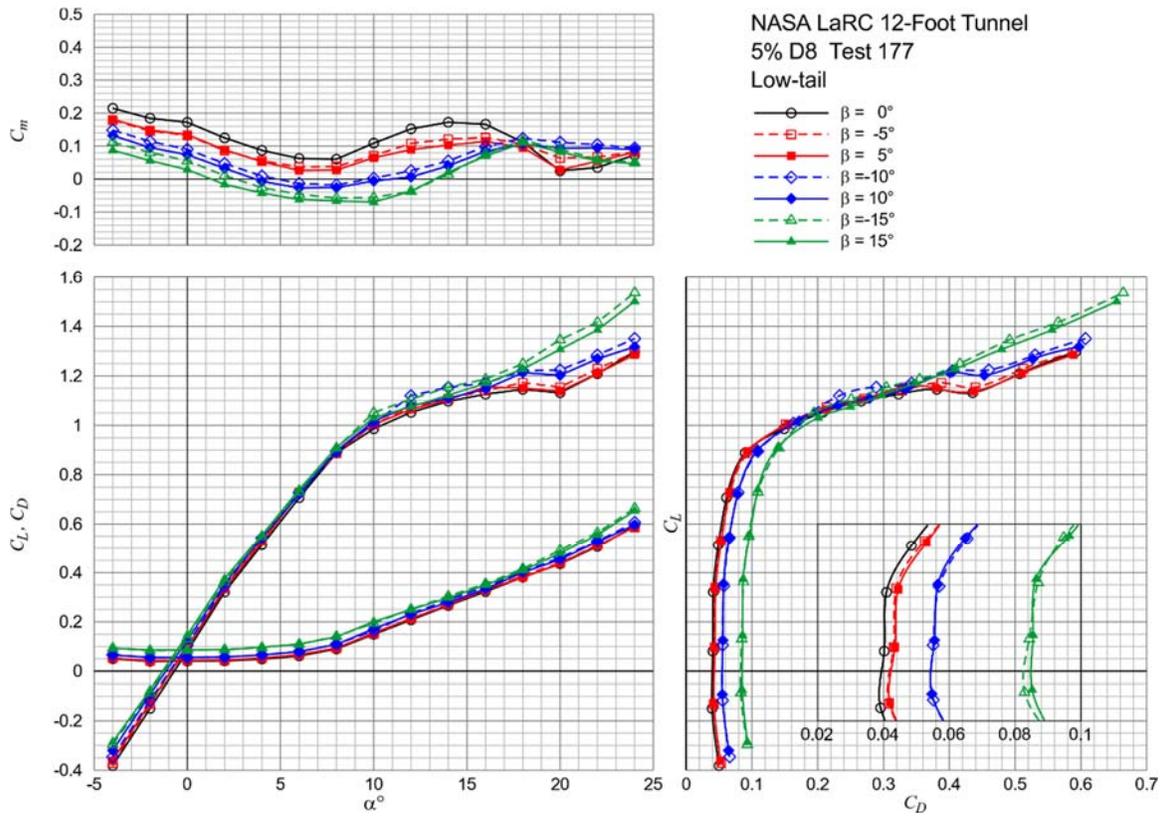
Figure 19 – Effect of sideslip angle on longitudinal coefficients of the Low-tail configuration.
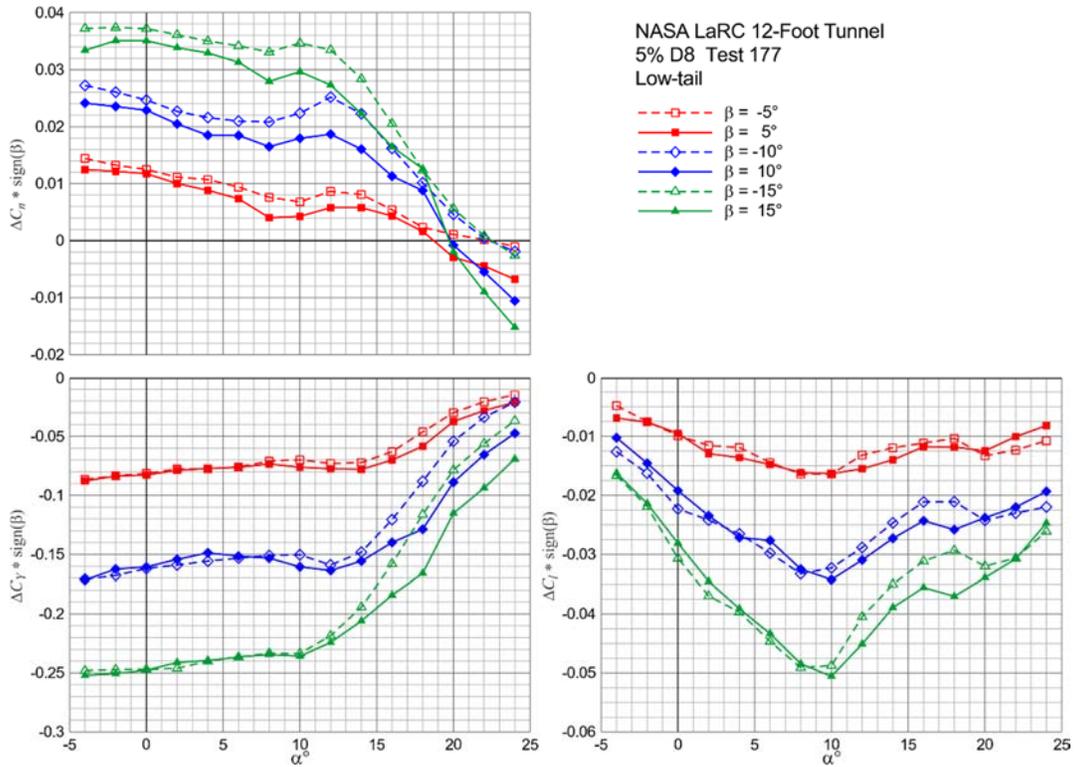
Figure 20 – Change in lateral/directional coefficients of the Low-tail configuration with angle of attack.
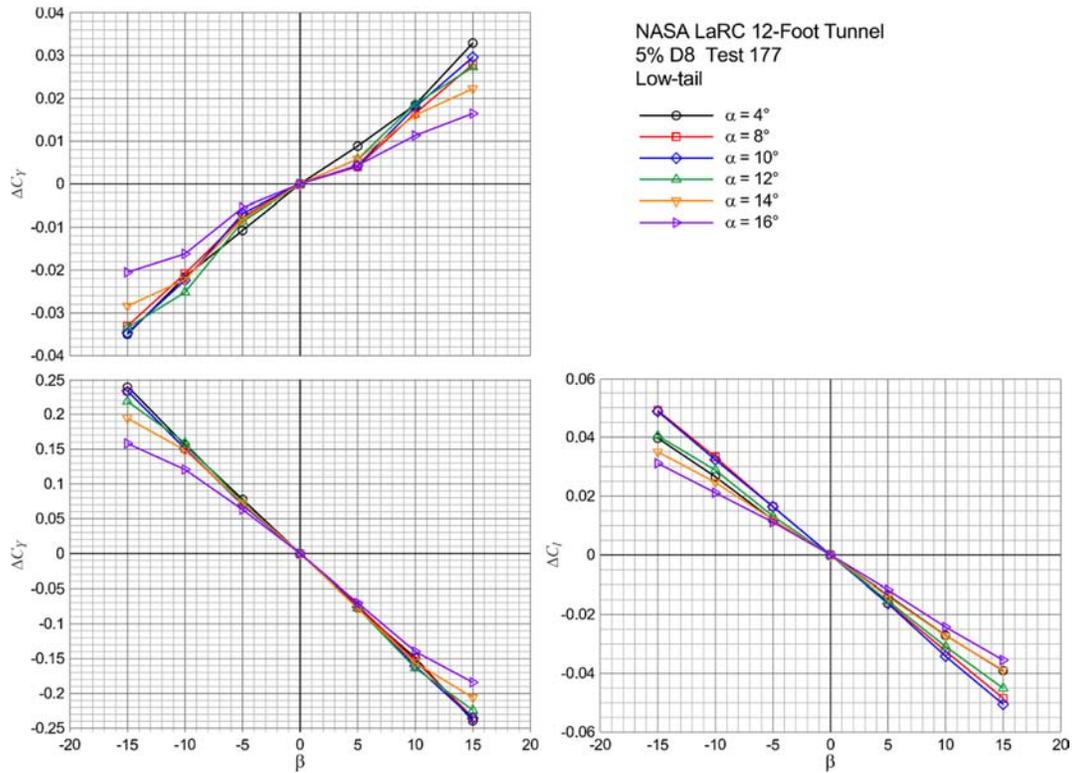
Figure 21 – Change in lateral/directional coefficients of the Low-tail configuration with sideslip angle.

17

No-tail Configuration

The No-tail configuration was tested for comparison with the other empennage configurations and is shown mounted in the tunnel in figure 22. The corresponding force and moment coefficients over the nominal angle of attack and sideslip range are presented in figures 23 and 24. Direct comparisons of the No-tail configuration with the other empennage configurations are presented in the next section.

Figure 22 – Aft view of No-tail configuration in the tunnel.
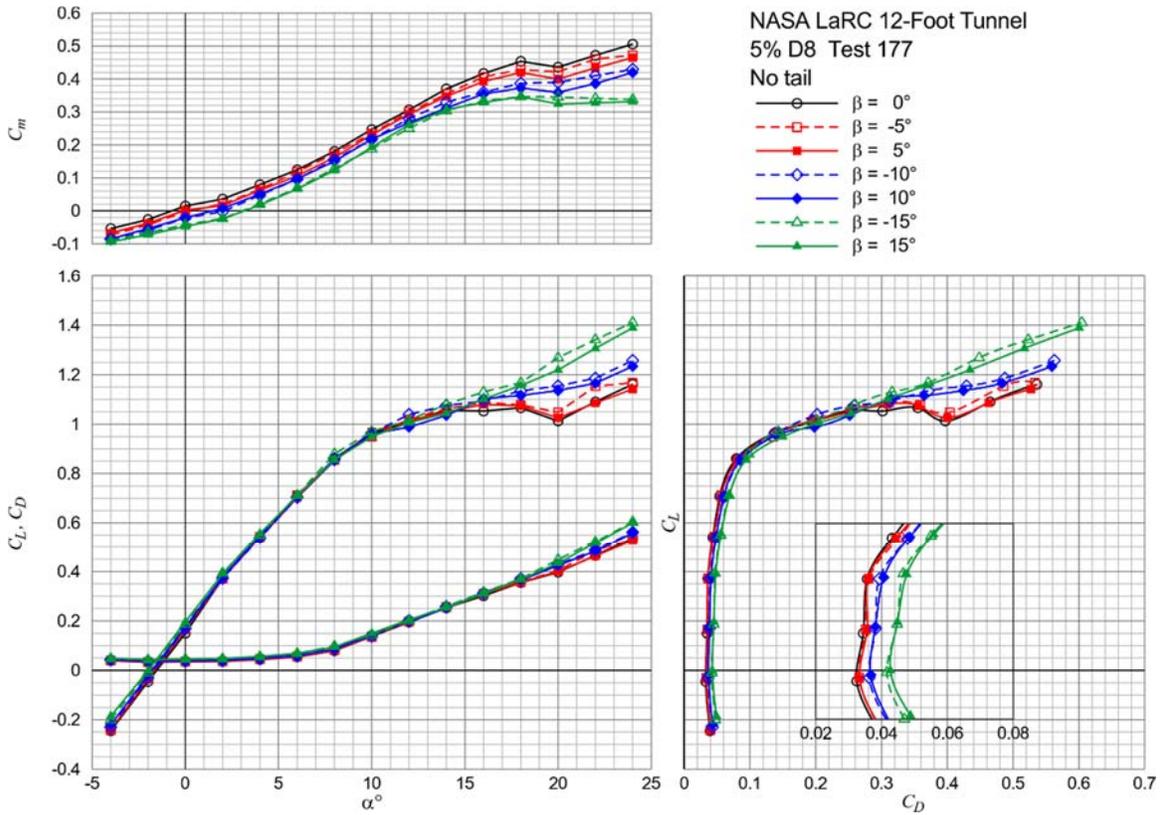
Figure 23 – Effect of sideslip angle on longitudinal coefficients of the No-tail configuration.
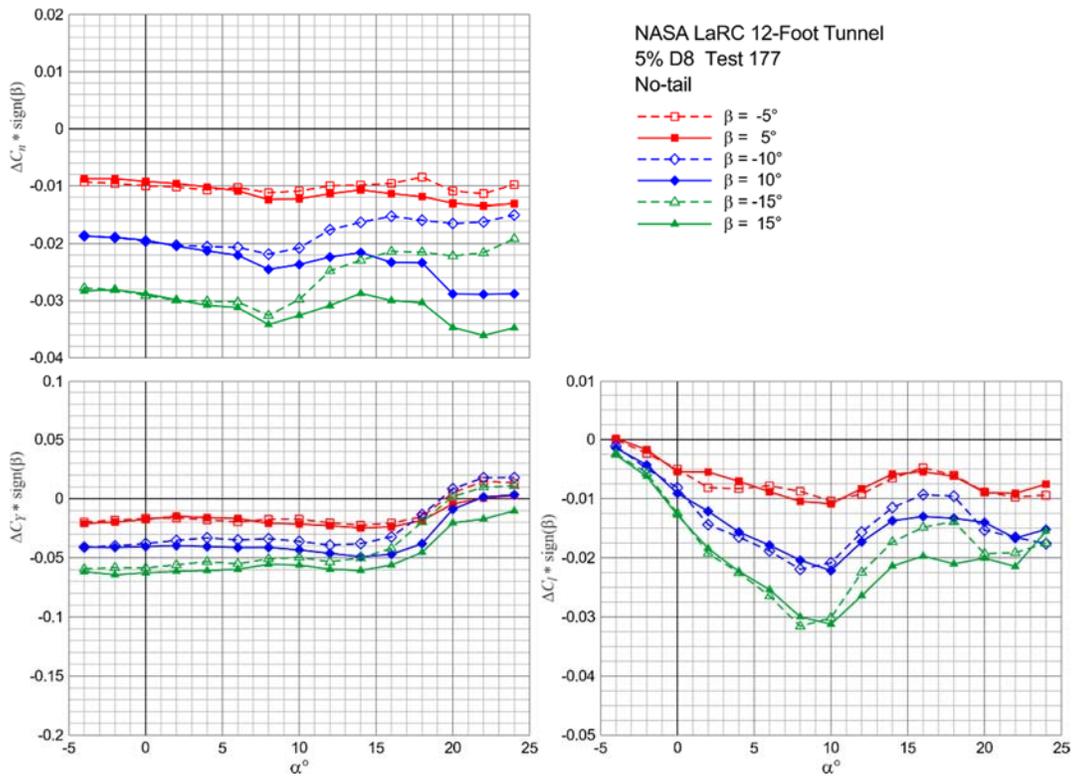
Figure 24 – Change in lateral/directional coefficients of the No-tail configuration with angle of attack.

Tail Comparison

Direct comparisons of the different empennage configurations tested are presented in figures 25 thru 29. Comparison of the longitudinal coefficients over the nominal and large angle of attack ranges are shown in figures 25 and 26, respectively. Both the Pi-tail and Low-tail configurations produced an increase in the lift curve slope and increased the minimum drag over the No-tail configuration. The Low-tail configuration produced the higher lift at the extreme angle of attack.

The pitching moment reveals the most dramatic difference. As one might expect, the No-tail empennage produced an unstable pitch slope over the angle of attack range tested. The Pi-tail provided a more stable pitch slope than the Low-tail from -4 to 8 degrees angle of attack. This is more clearly shown with the static margin parameter ($\frac{\partial C_m}{\partial C_L}$) for the three tail configurations presented in figure 27. Although the Low-tail and Pi-tail have the same tail span, the Pi-tail has about 1.7 times more (exposed) horizontal surface area, which would account for some of the increased pitch stability. Both tail configurations had zero stabilizer and elevator deflections.
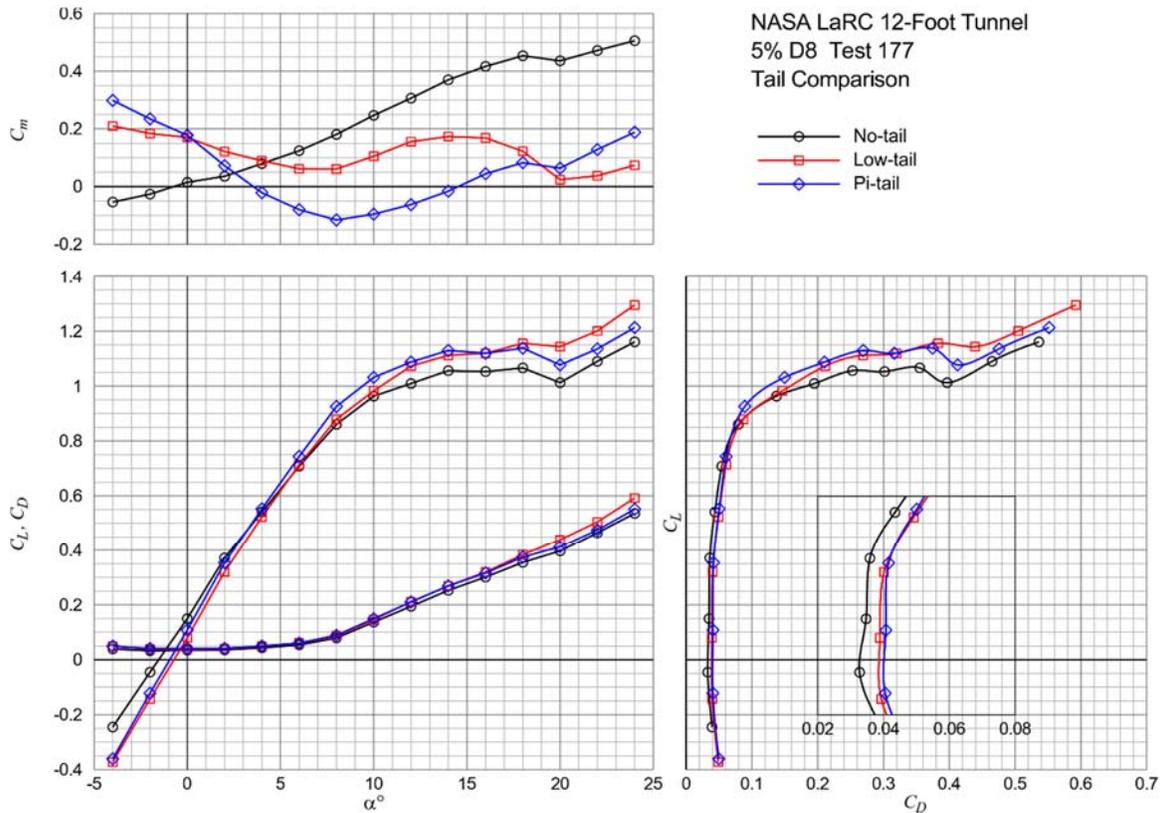
Figure 25 – Longitudinal coefficient comparison of the three tail configurations.
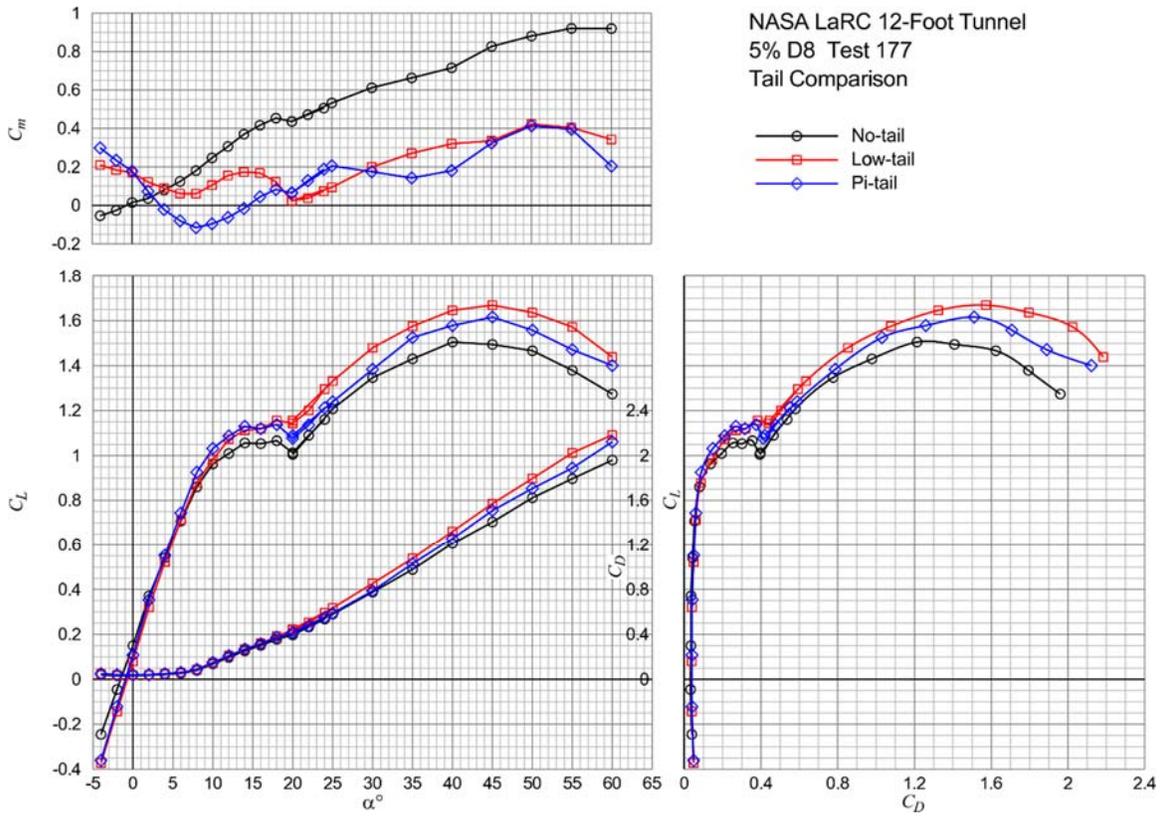
Figure 26 – Longitudinal coefficient comparison of the three tail configurations over a large angle of attack range.
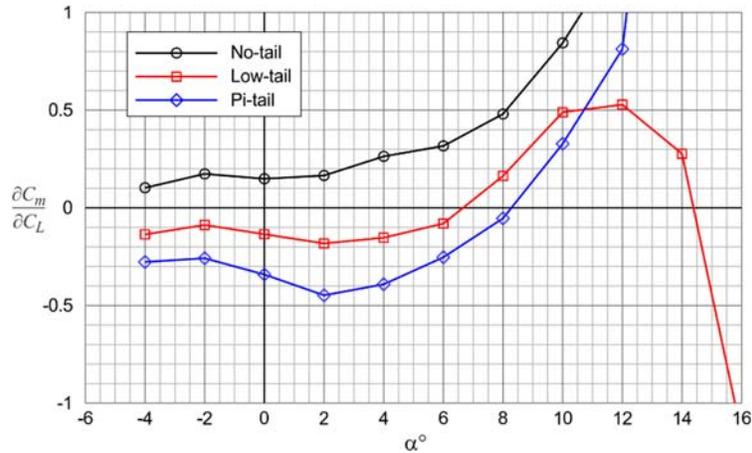

Figure 27 – Pitch stability comparison of the three tail configurations.

The lateral/directional effects of the different empennage configurations are presented in figures 28 and 29 over the nominal angle of attack range at fixed sideslip angles. Figure 28 shows the average of the coefficient changes from the positive and negative sideslip values presented in figures 15, 20 and 24. For example:

$$[\Delta C_n * \text{sign}(\beta = \pm 5°)]_{avg} = \frac{1}{2}[\Delta C_n * \text{sign}(\beta = -5°) + \Delta C_n * \text{sign}(\beta = +5°)]$$

   The No-tail values are presented with the small solid symbols and dash dot lines, the Low-tail values are shown with the open symbols and the dashed lines, and the Pi-tail values are the solid symbols with the solid lines. The figure shows that the Low-tail provided slightly better directional stability at the larger sideslip angles. The Pi-tail produce more rolling moment with sideslip than the Low-tail. The larger surface area of the Pi-tail swept stabilizer, as well as the large vertical moment arm relative to the Low-tail configuration, may account for this increased rolling moment.

   Figure 29 shows the lateral/directional sideslip derivatives for each of the tail configurations as well as the effect of the alternate nose. The sideslip derivatives were computed as the central difference of the +5 and -5 degree sideslip values at each angle of attack. The figure shows that the configuration is directionally stable up to about 20 degrees angle of attack with either the Low-tail or Pi-tail. The nose shape did not have a significant effect. The vertical fins of the Low-tail configuration appear to be slightly more effective. The capping of the vertical fins with the Pi-tail stabilizer may have reduced the vertical fin efficiency.
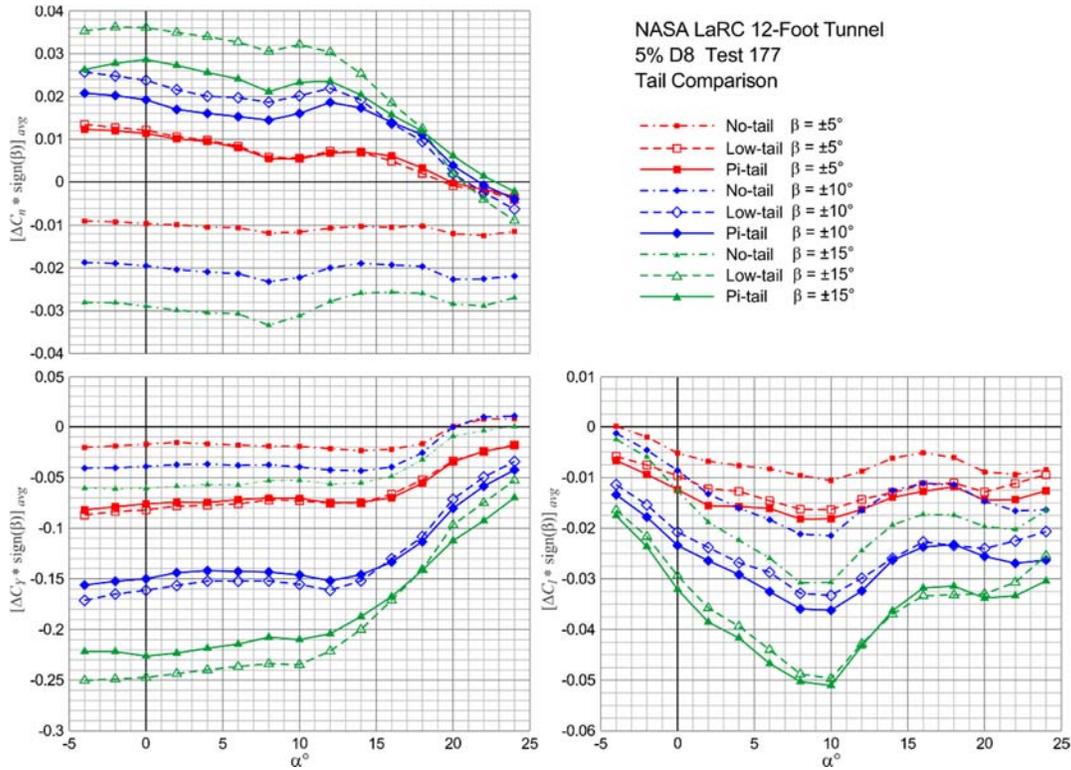
Figure 28 – Comparison of the average change in lateral/directional coefficient times sign of the sideslip angle.
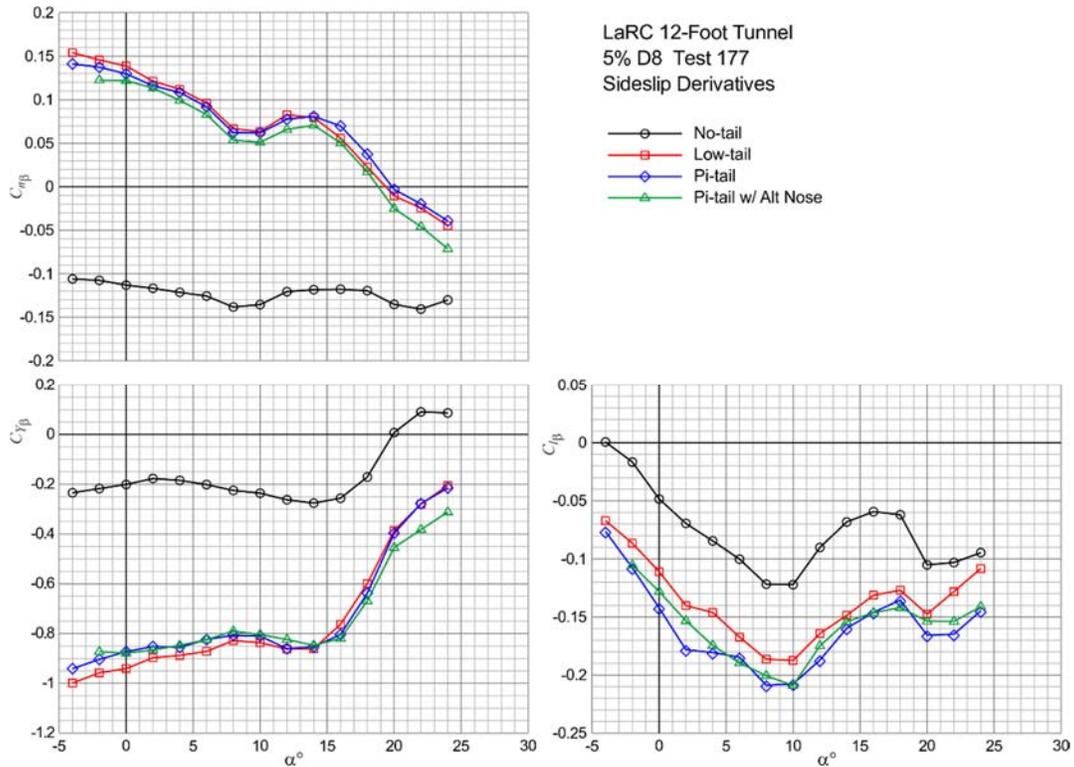
Figure 29 – Lateral/directional sideslip derivatives for each empennage configuration.

Control Effectiveness

The control effectiveness is presented as the change in the coefficient values from the undeflected condition at the same angle of attack and sideslip.

Stabilizer Effectiveness

The original model Pi-tail was fabricated with the stabilizer fixed at 0° of deflection. The tail was later modified to include stabilizer deflections of -15°, -10°, -5° and 5° by cutting the vertical fins at the top of the rudder and fabricating new deflected stabilizer parts that included the vertical fin tips. A check of the unmodified and modified 0° stabilizer runs showed a shift in the pitching moment. This shift was likely due to a stabilizer incidence shift when remounting on the modified tail. Because of this difference all of the stabilizer effectiveness increments were computed relative to the modified 0° stabilizer runs.

The effects of stabilizer deflection angle on the longitudinal coefficients are shown in figures 30 thru 32. Figure 30 shows the total coefficient values over a large angle of attack range whereas figure 31 shows the change in coefficient relative to the 0° stabilizer values. Figure 32 shows these same stabilizer control increments as a function of stabilizer deflection at fixed angles of attack. The pitching moment and lift increments are fairly linear with control deflection even at the higher angles of attack.

23
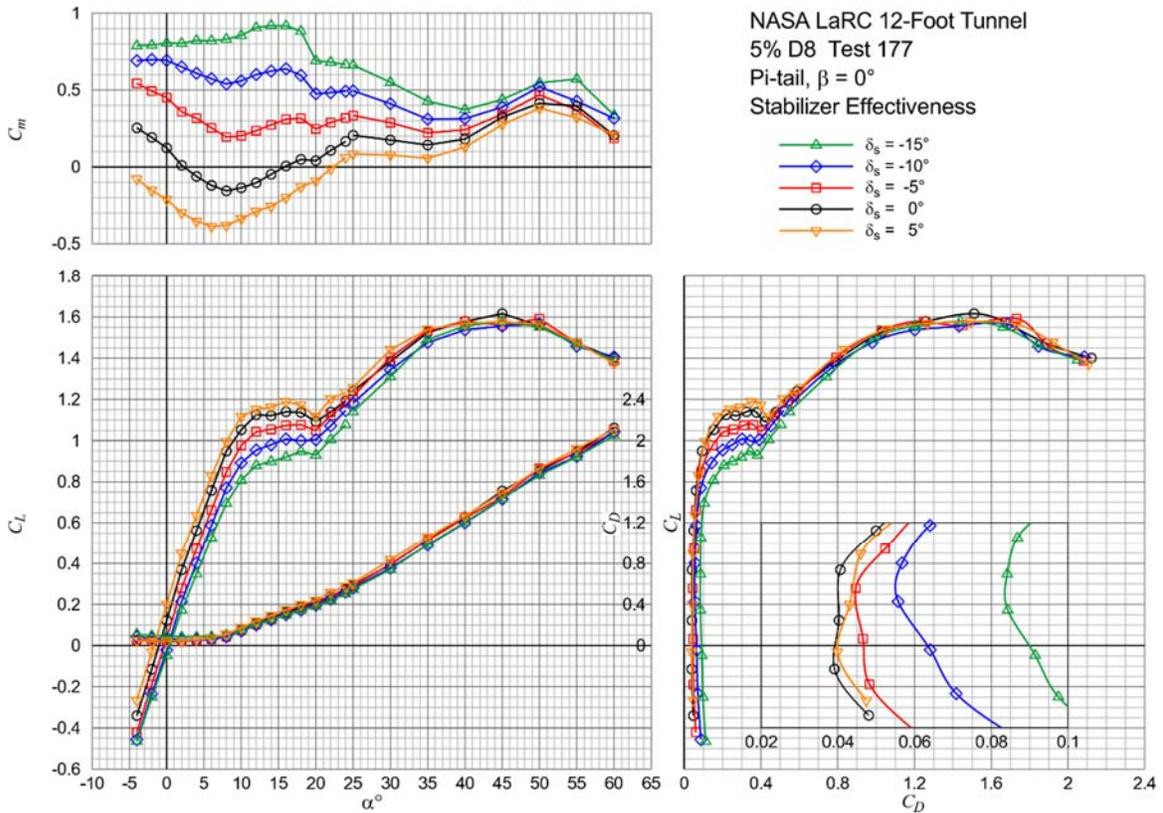
Figure 30 – Effect of stabilizer deflection on Pi-tail longitudinal coefficients over a large angle of attack range
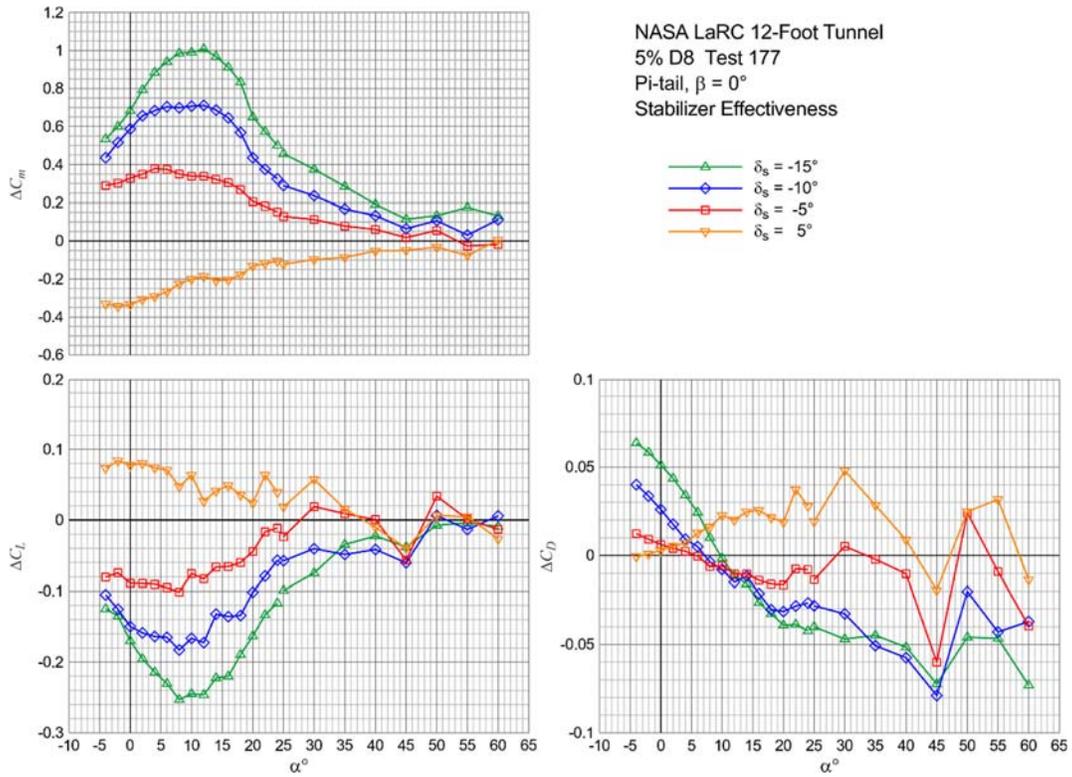

Figure 31 – Pi-tail stabilizer longitudinal control increments over a large angle of attack range.

24
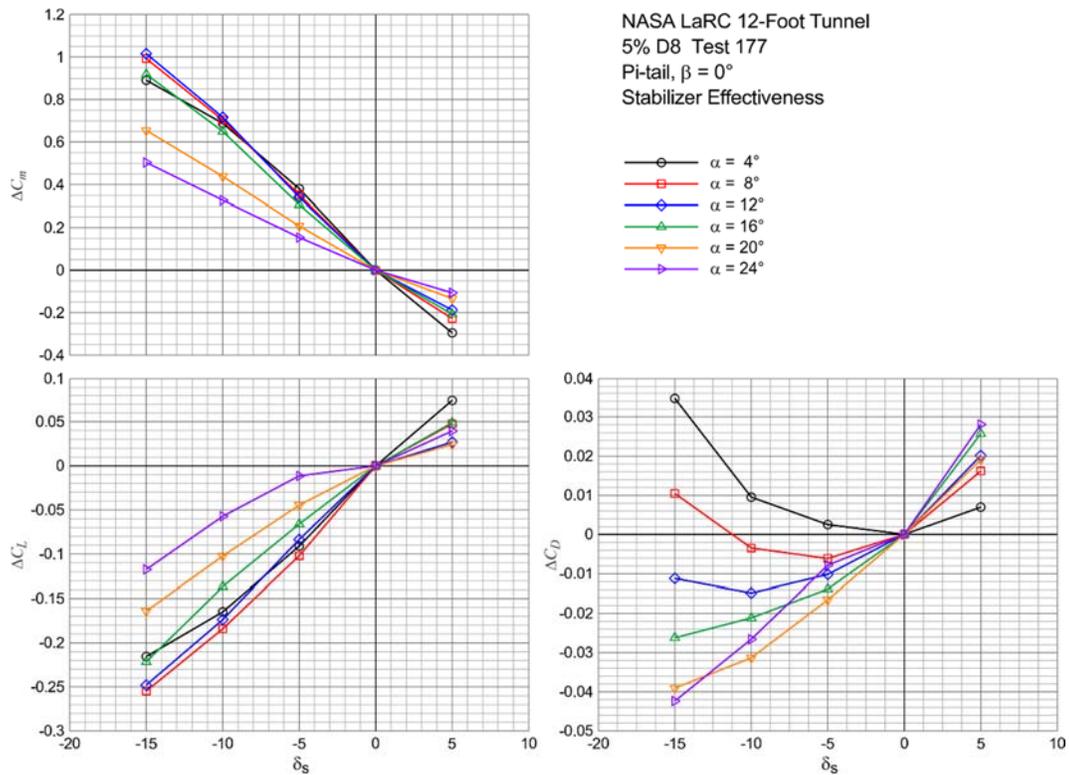
Figure 32 – Pi-tail stabilizer control increments with control deflection at fixed angles of attack.

The stabilizer lift and drag increments presented in figure 31 have some noticeable irregular fluctuations with angle of attack. Figure 33 shows the complementary normal and axial force coefficient increments from which the lift and drag increments are derived. It is apparent that the lift and drag fluctuations are originating from the fluctuations in the normal coefficient increments. The axial coefficient increments are fairly smooth with angle of attack. The root cause of the normal force fluctuations is unknown at this time. Some of the potential causes are tunnel turbulence, insufficient data sampling interval or balance and model structural interaction.
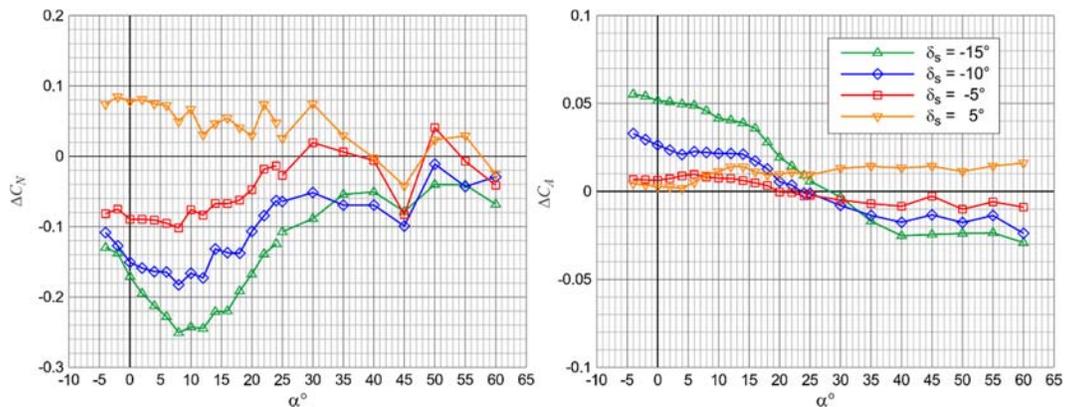
Figure 33 – Pi-tail stabilizer normal and axial control increments over a large angle of attack range.

An alternate normal force increment can be derived from the smoother pitching moment and axial force increments if the distance from the stabilizer aerodynamic center and the moment reference center are known.

$$\Delta C_m = \Delta C_A \bar{z}_s - \Delta C_N \bar{x}_s \qquad (1)$$

Where $\qquad\qquad \bar{x}_s = (x_{mrc} - x_{ac})/\bar{c} \;\; and \;\; \bar{z}_s = (z_{mrc} - z_{ac})/\bar{c} \qquad (2)$

The vertical distance between the stabilizer aerodynamic center and the moment reference center can be considered to be fairly constant ($\bar{z}_s$). However, the horizontal location of the stabilizer aerodynamic center (x_{ac}) may vary with angle of attack. If the stabilizer vertical aerodynamic center is assumed to be coincident with the stabilizer rotation axis then the nondimensional vertical moment arm is:

$$\bar{z}_s \approx 1.49 \qquad (3)$$

The nondimensional horizontal moment arm values computed from equation 1 and the stabilizer control increments presented in figures 31and 33 are shown in figure 34. A linear fit of the values that lie within the geometric limits of the stabilizer is also shown and presented as equation 4.
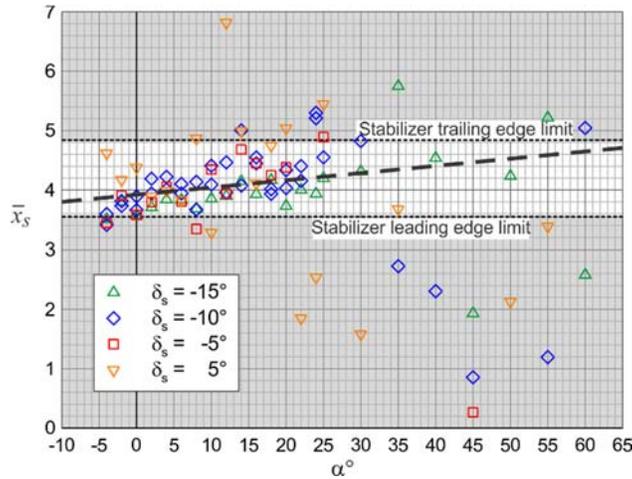
Figure 34 – Linear fit of nondimensional horizontal moment arm derived from Pi-tail stabilizer control increments.

$$\bar{x}_s = 0.0118\alpha + 3.923 \qquad (4)$$

A new set of normal, lift and drag increments were computed using the moment arm values of equations 3 and 4 and the pitching moment and axial coefficient increments. These new values are presented in figure 35 as dashed lines along with the original values shown as symbols. This moment arm fitting method appears to be a good way to smooth the fluctuations in the lift and drag increments.
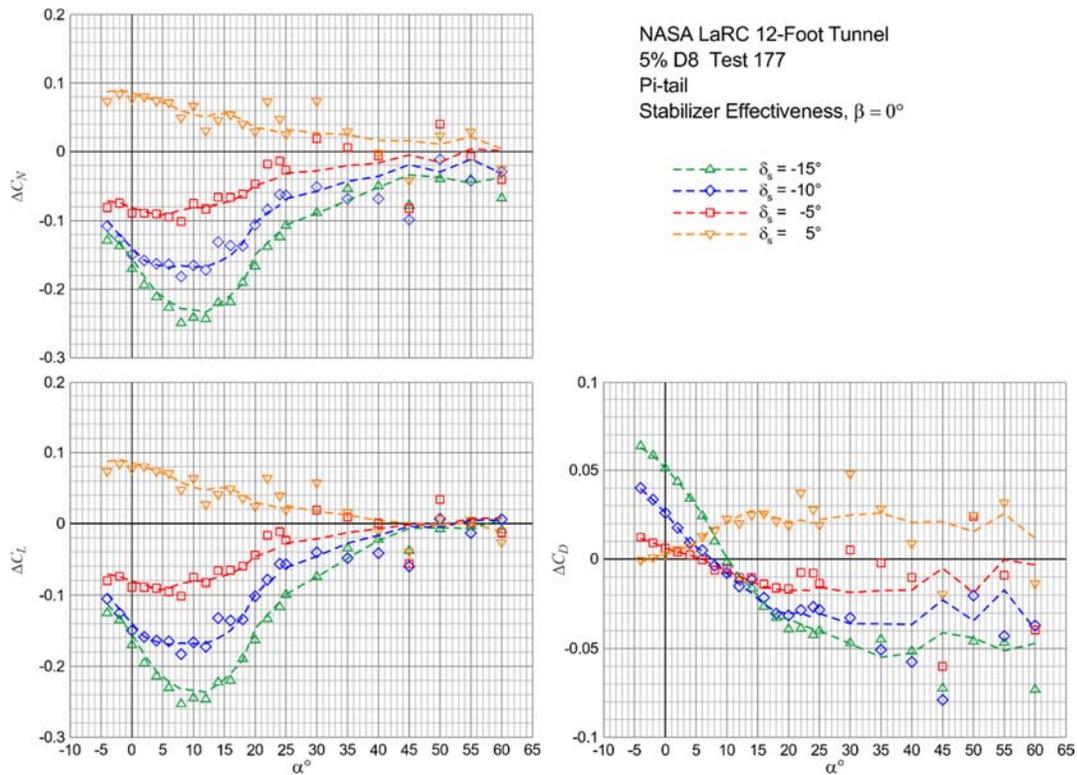
Figure 35 – Stabilizer normal, lift and drag increments with moment arm based fit values (dashed lines).

The effects of sideslip angle on the stabilizer control increments are shown in figures 36 and 37 for a -15° stabilizer deflection. The effects on the longitudinal control increments, shown in figure 36, are most apparent at sideslip angles beyond 5 degrees. The effects on the lateral/directional control increments, shown in figure 37 are small.
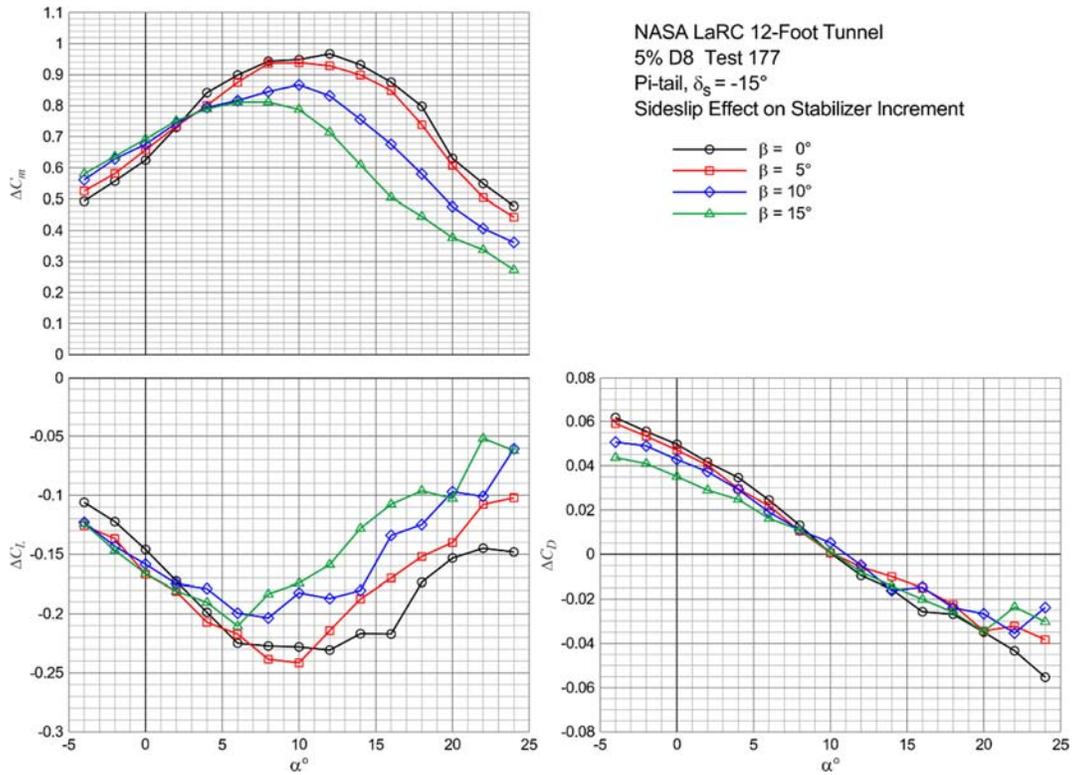
Figure 36 – Longitudinal control increments at fixed sideslip angles for Pi-tail stabilizer at -15° deflection.
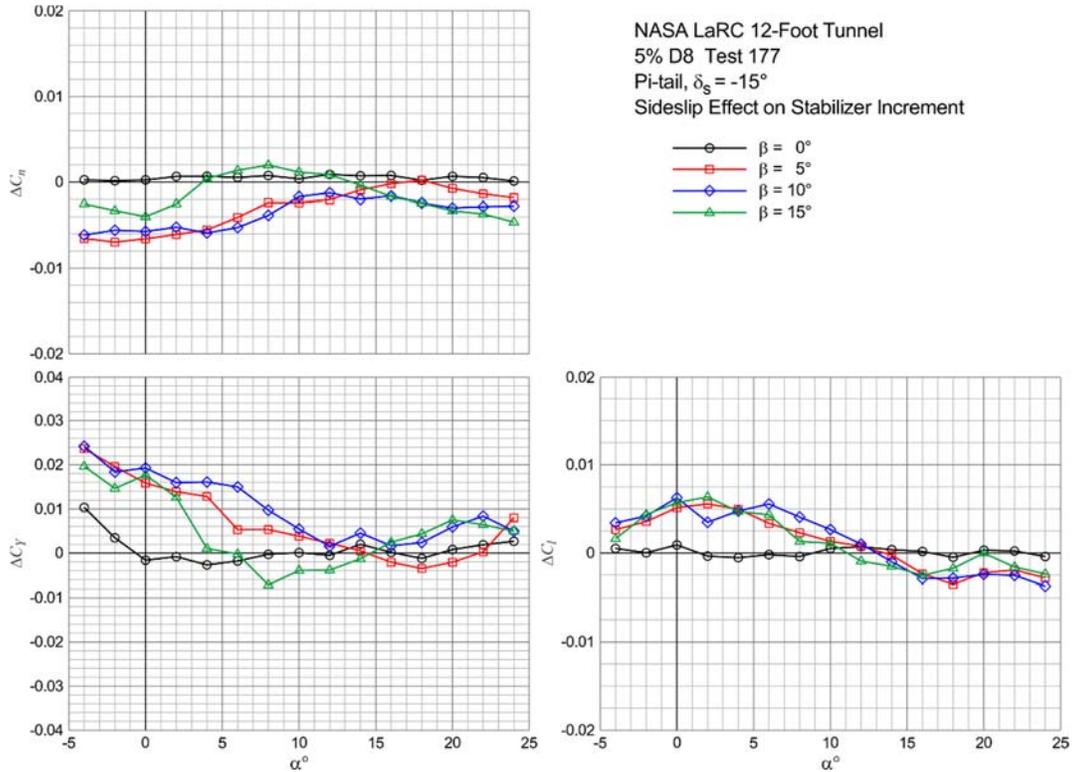
Figure 37 – Lateral/directional control increments at fixed sideslip angles for Pi-tail stabilizer at -15° deflection.

Elevator Effectiveness

The Pi-tail elevator longitudinal control increments with 0° of stabilizer deflection are shown in figure 38. The pitching moment increments are fairly constant over a large angle of attack range. The lift and drag increments show similar irregular fluctuations as those seen in the stabilizer increments of figure 31. Figure 39 shows the corresponding body axis increments. Again the irregular fluctuations reside in the normal force coefficient increments. The axial force and pitching moment are fairly smooth with angle of attack. The horizontal moment arm of the elevator was computed applying the same approach used with the stabilizer. The resulting elevator moment arm values and are shown in figure 40.
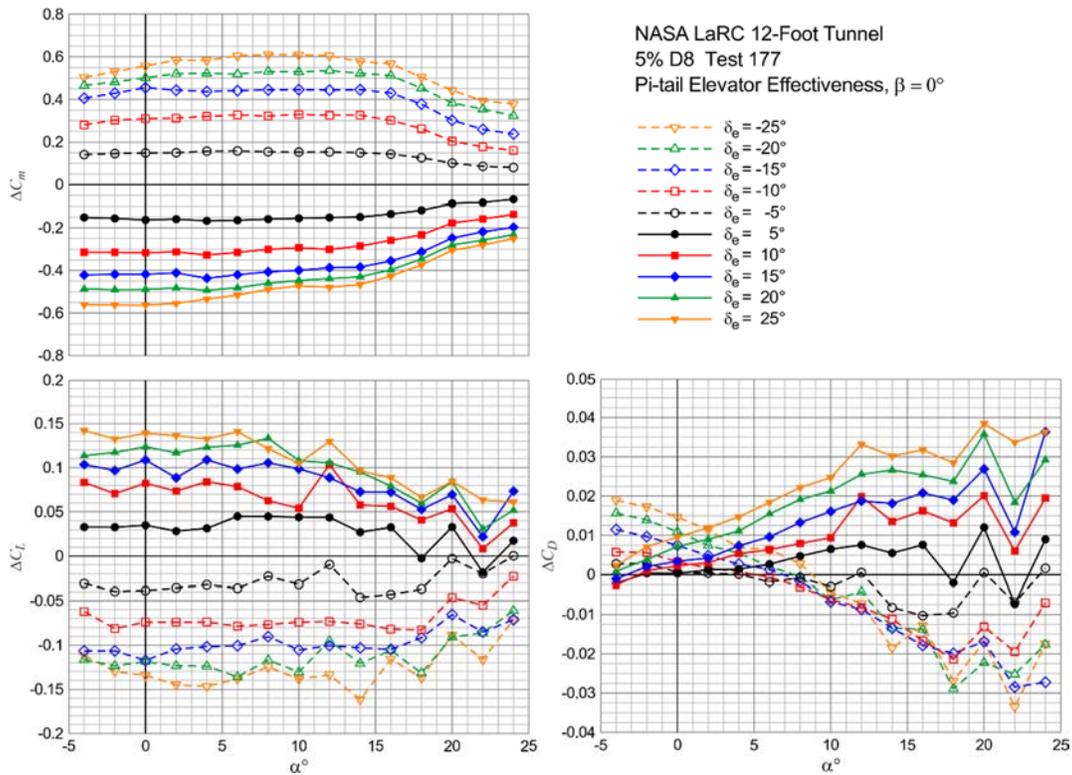
Figure 38 – Pi-tail elevator longitudinal control increments for 0° stabilizer deflection.
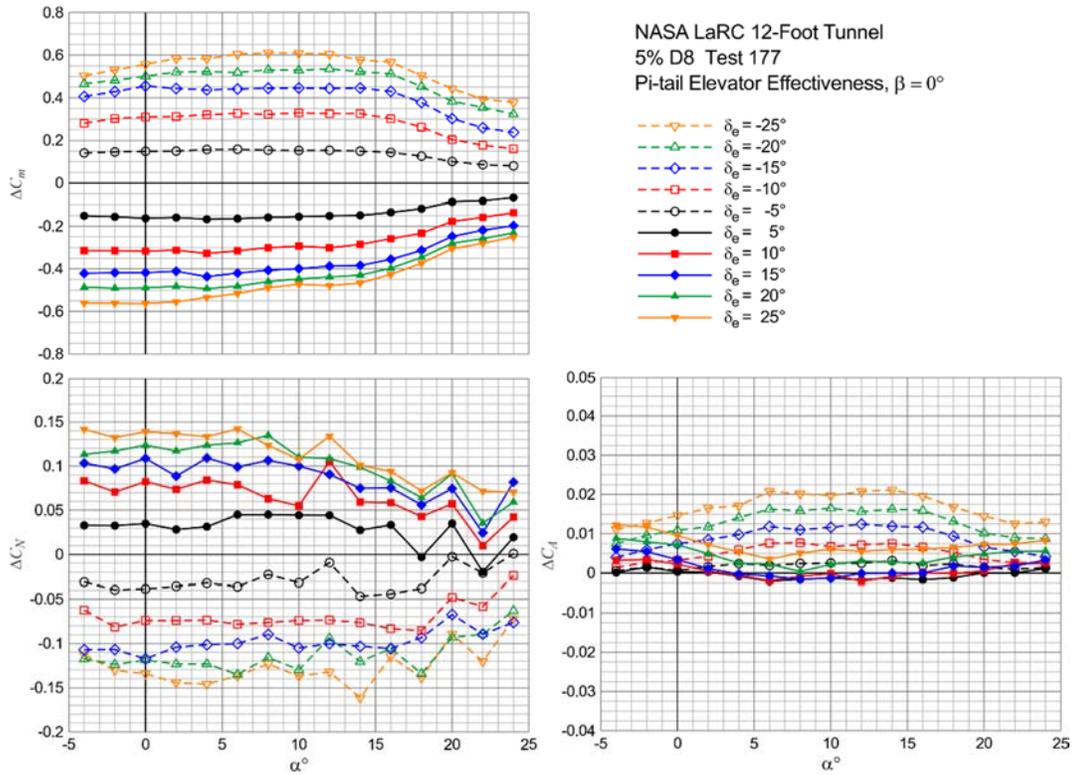
Figure 39 – Pi-tail elevator longitudinal body axis control increments for 0° stabilizer deflection.
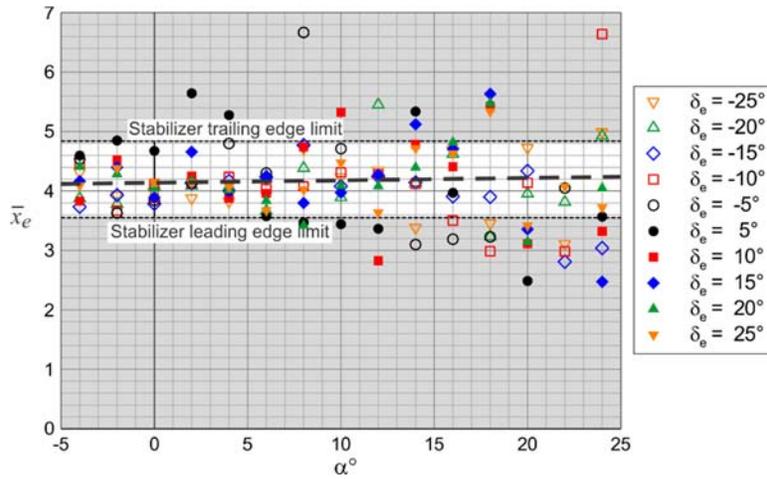
Figure 40 – Linear fit of nondimensional horizontal moment arm derived from Pi-tail elevator control increments.

$$\bar{x}_e = 0.0039\alpha + 4.1374 \qquad (5)$$

A new set of normal, lift and drag increments were computed using the moment arm values of equations 3 and 5 and the pitching moment and axial coefficient increments. These new values are presented in figure 41 as lines and dashed lines along with the original values shown as symbols.

The elevator control increments as a function of elevator deflection angle on the longitudinal coefficients are shown in figure 42 for several fixed angles of attack values. Also shown for the lift and drag increments are the moment arm fit values presented as dashed lines. The pitching moment increments are fairly linear within ±10° of elevator deflection even at the higher angles of attack.

30
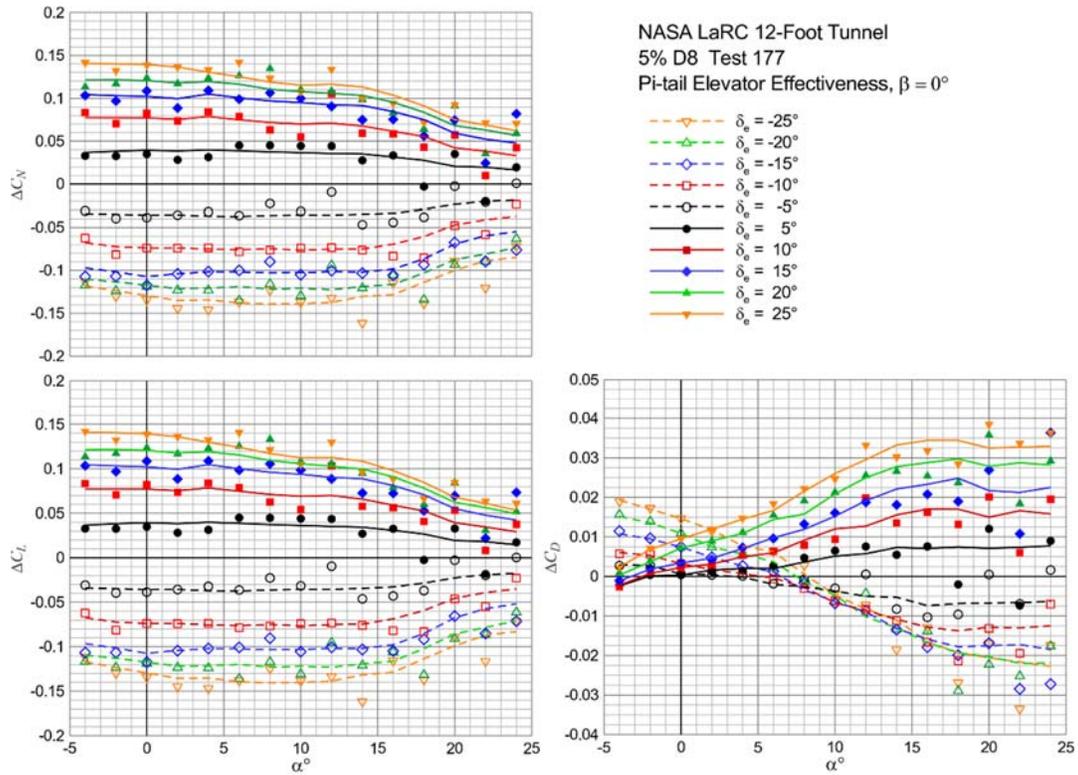
Figure 41 – Pi-tail elevator normal, lift and drag increments with moment arm based fit values (lines).
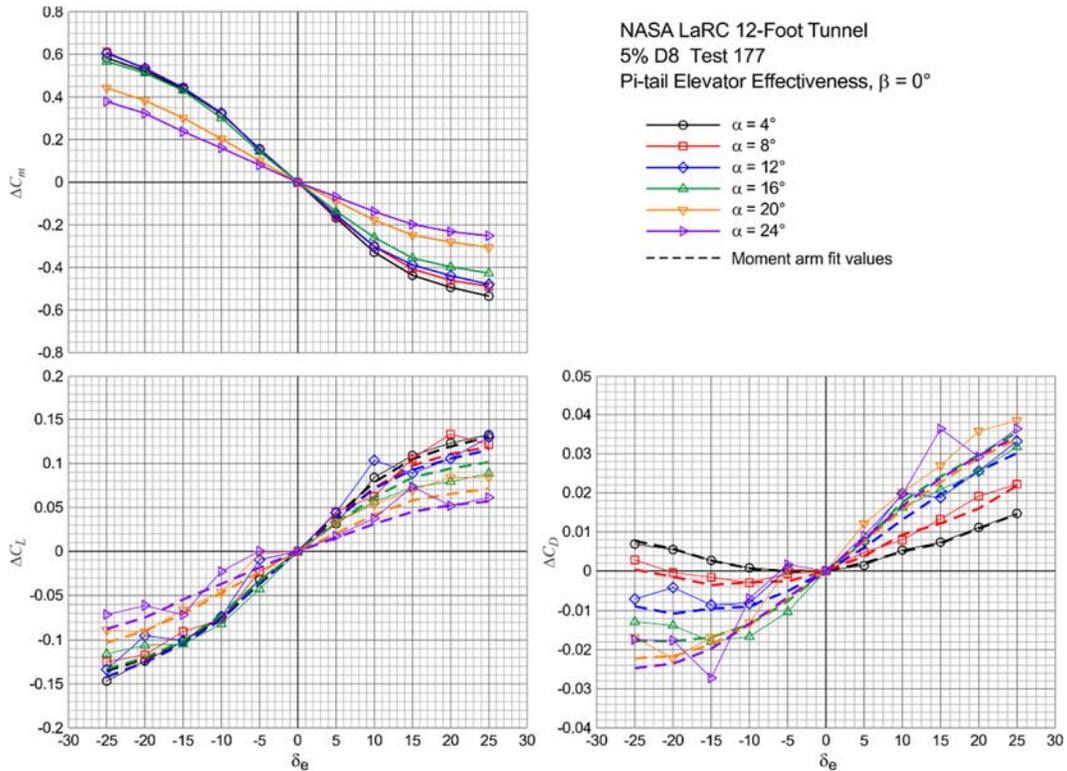

Figure 42 – Pi-tail elevator longitudinal control increments with elevator deflection at fixed angles of attack.

The effect of stabilizer deflection on the elevator effectiveness at 4° angle of attack is presented in figure 43. The elevator effectiveness diminishes slightly at the largest stabilizer deflection of -15°. There is also a large change in elevator control increments between 15° and 25° of elevator deflection for the 5° and -15° stabilizer deflection cases. This may be indicative of flow separation over the control surface.
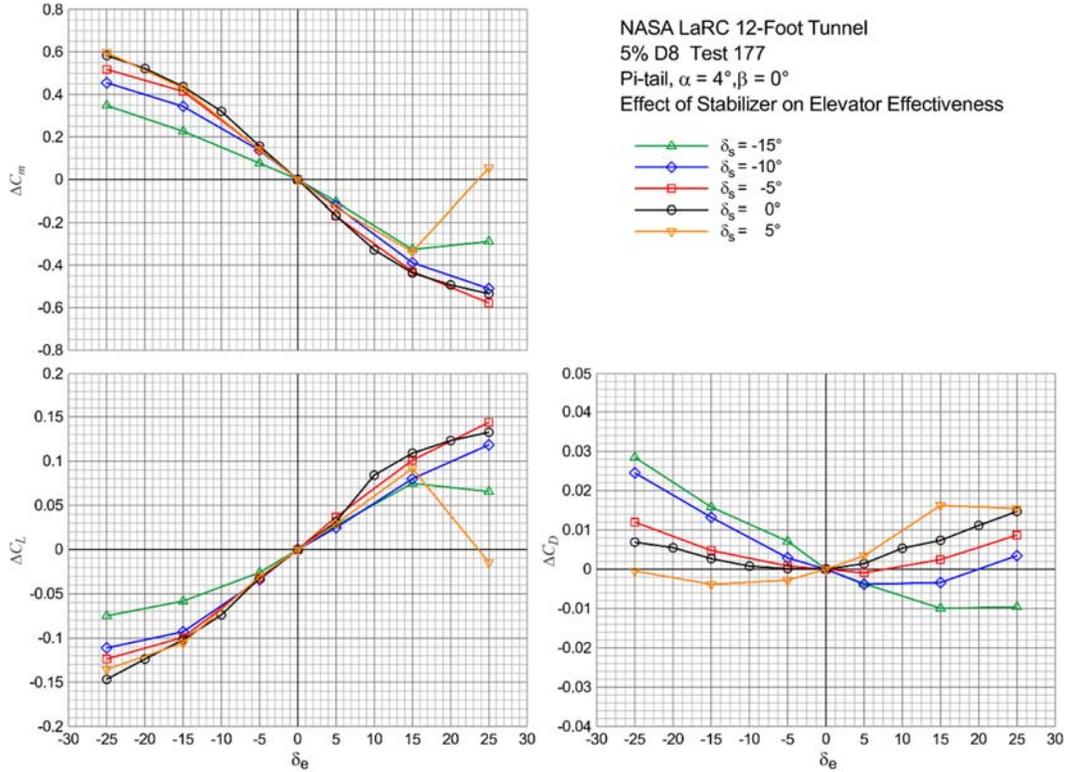
Figure 43 – Pi-tail elevator longitudinal control increments with elevator deflection at fixed stabilizer angles.

The elevator effectiveness with angle of attack at stabilizer deflections of -15°, -10°, -5° and 5° are presented in figures 44 thru 47, respectively. The lines presented in the lift and drag increments are from the moment arm fit values. The symbols are the measured values. A linear fit of the moment arm values was computed for each stabilizer deflection since the elevator effective moment arm may vary with stabilizer deflection. The resultant values are presented in table 3.

Table 3 – Elevator horizontal moment arm fit values.

δ_s	$\overline{x}_e$
-15°	$-0.0035\alpha + 4.1261$
-10°	$-0.0007\alpha + 4.0784$
-5°	$0.0026\alpha + 4.0786$
0°	$0.0039\alpha + 4.1374$
5°	$0.0006\alpha + 4.1247$

The 25° elevator deflection cases shown in figures 44 and 47 show that the diminished control effectiveness noted in figure 43 persists across the angle of attack range. This supports the premise that the flow is likely separated across the control surface at this relatively low test Reynolds number.
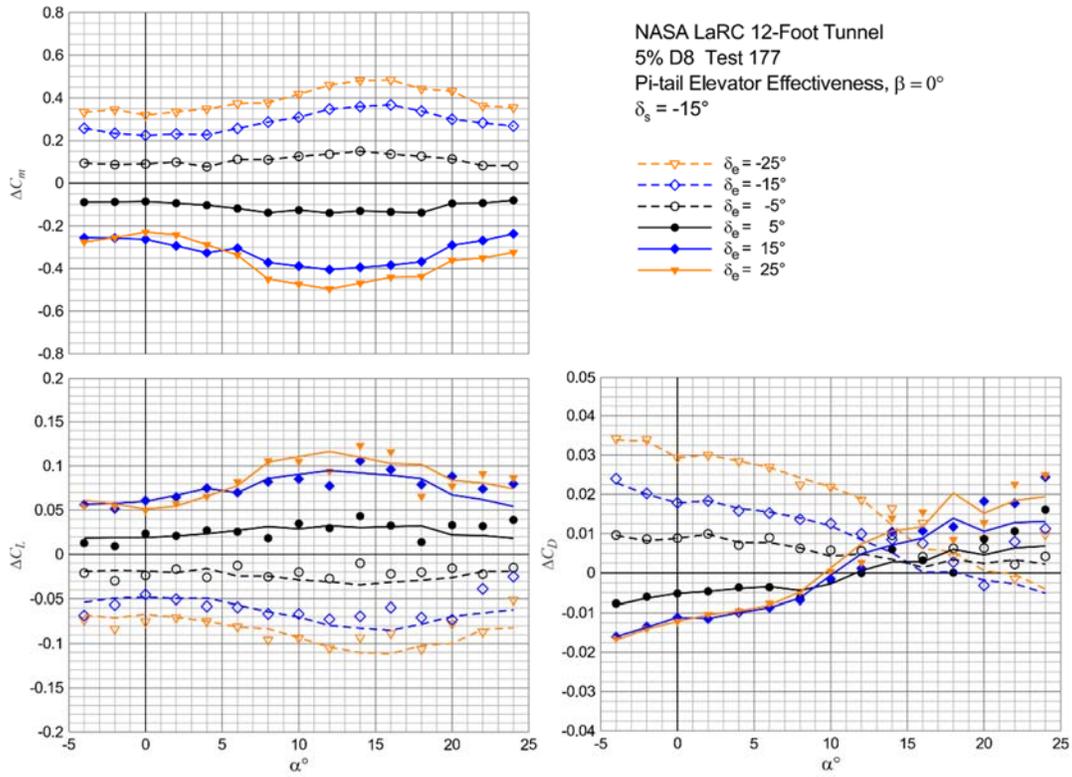
Figure 44 – Pi-tail elevator longitudinal control increments for -15° stabilizer deflection.
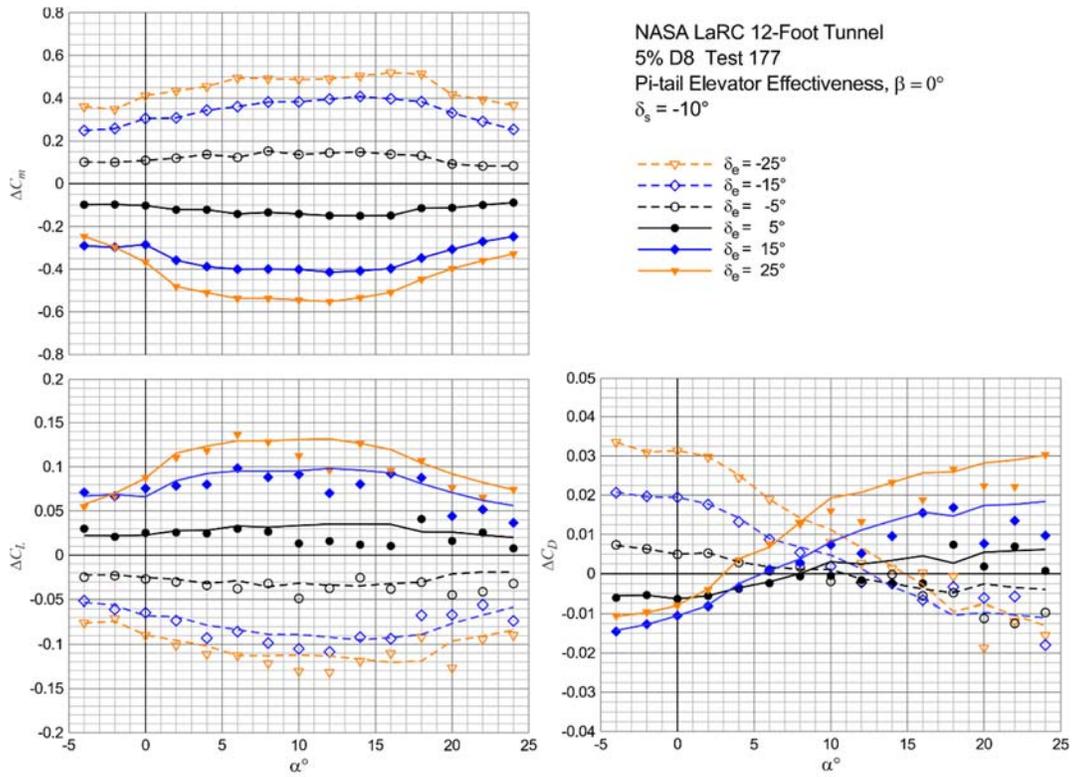
Figure 45 – Pi-tail elevator longitudinal control increments for -10° stabilizer deflection.
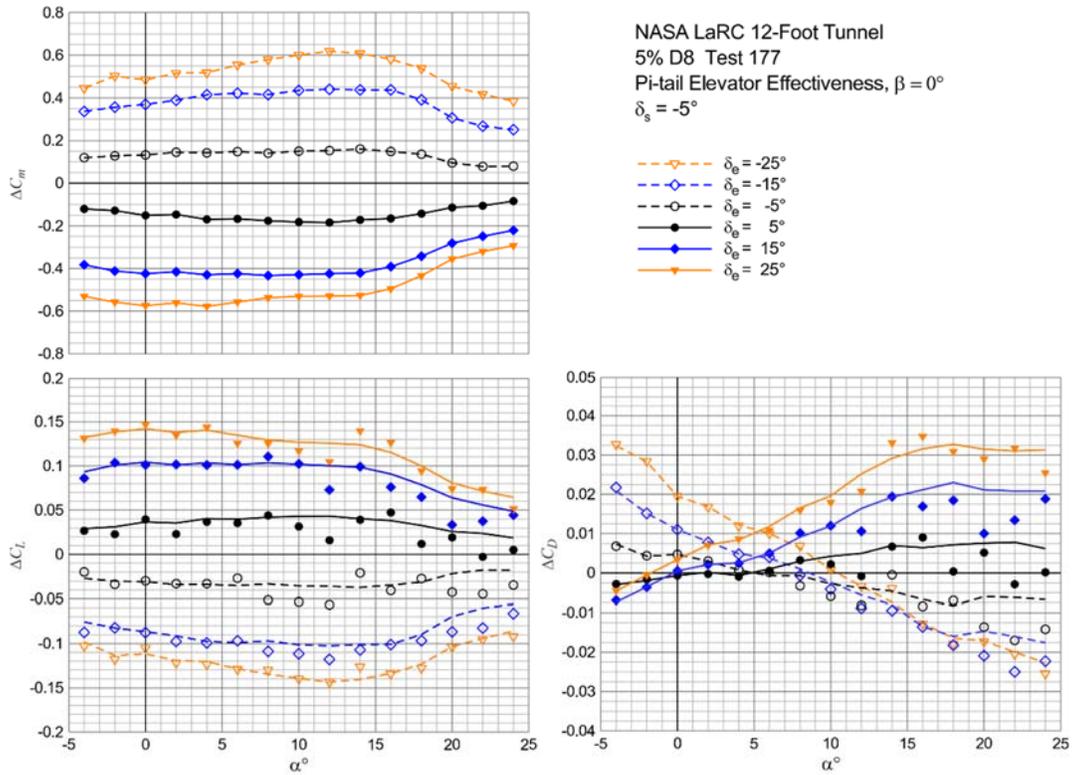
Figure 46 – Pi-tail elevator longitudinal control increments for -5° stabilizer deflection.
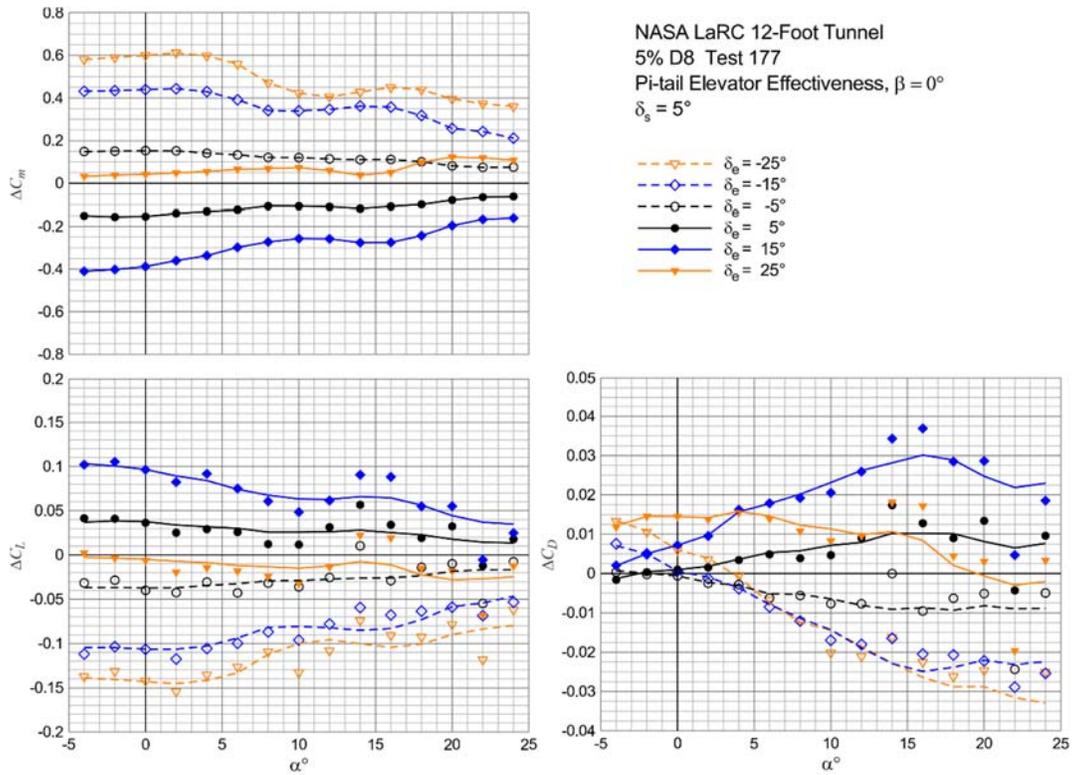
Figure 47 – Pi-tail elevator longitudinal control increments for 5° stabilizer deflection.

34

The effects of sideslip angle on the elevator effectiveness with 0° stabilizer deflection are presented in figures 48 thru 50. No moment arm fitting was done for the nonzero sideslip cases. The figures show a slight reduction in elevator effectiveness with sideslip.
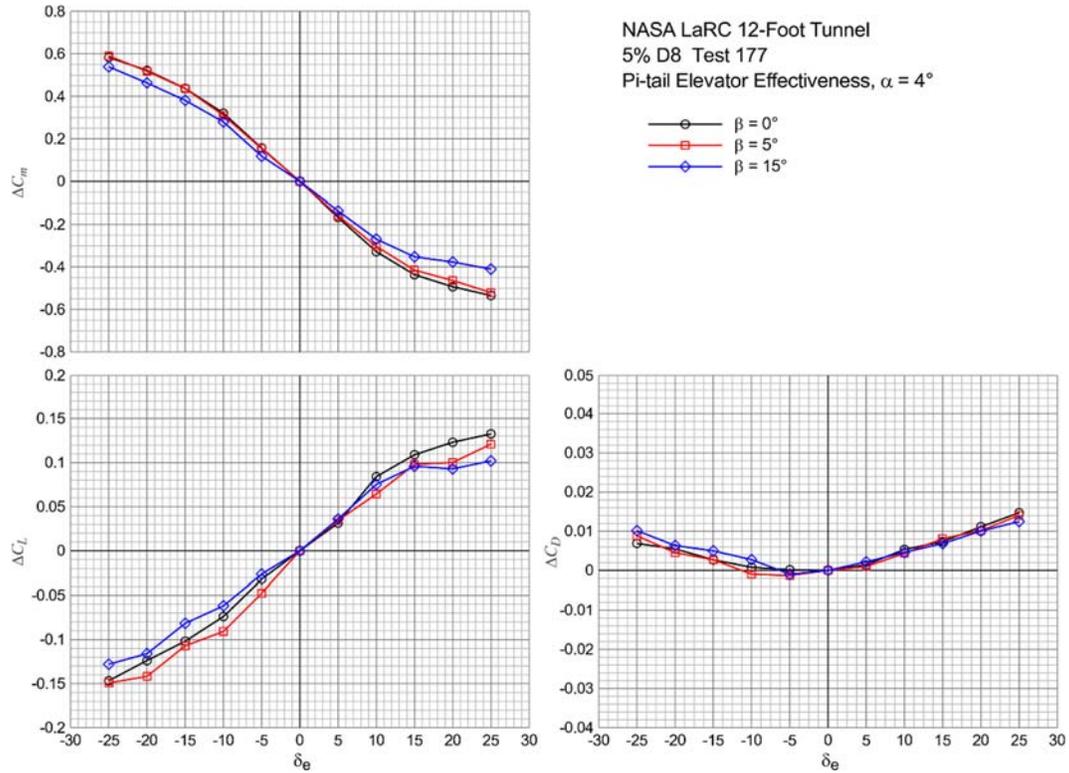

Figure 48 – Effect of sideslip angle on Pi-tail elevator longitudinal control increments.

A comparison of the elevator effectiveness of the Pi-tail and Low-tail is shown in figure 51. The Pi-tail elevator has slightly more than twice the pitching moment increment of the Low-tail elevator. This is primarily due to the Pi-tail elevator having 1.7 times more surface area and 1.4 times longer moment arm. The effective moment arm values for the Low-tail elevator are:

$$\bar{z}_s \approx 0.28 \tag{6}$$

$$\bar{x}_e = 0.0125\alpha + 3.0986 \tag{7}$$

The lines presented in the lift and drag increments of figure 51 are from the moment arm fit values. The symbols are the measured values.
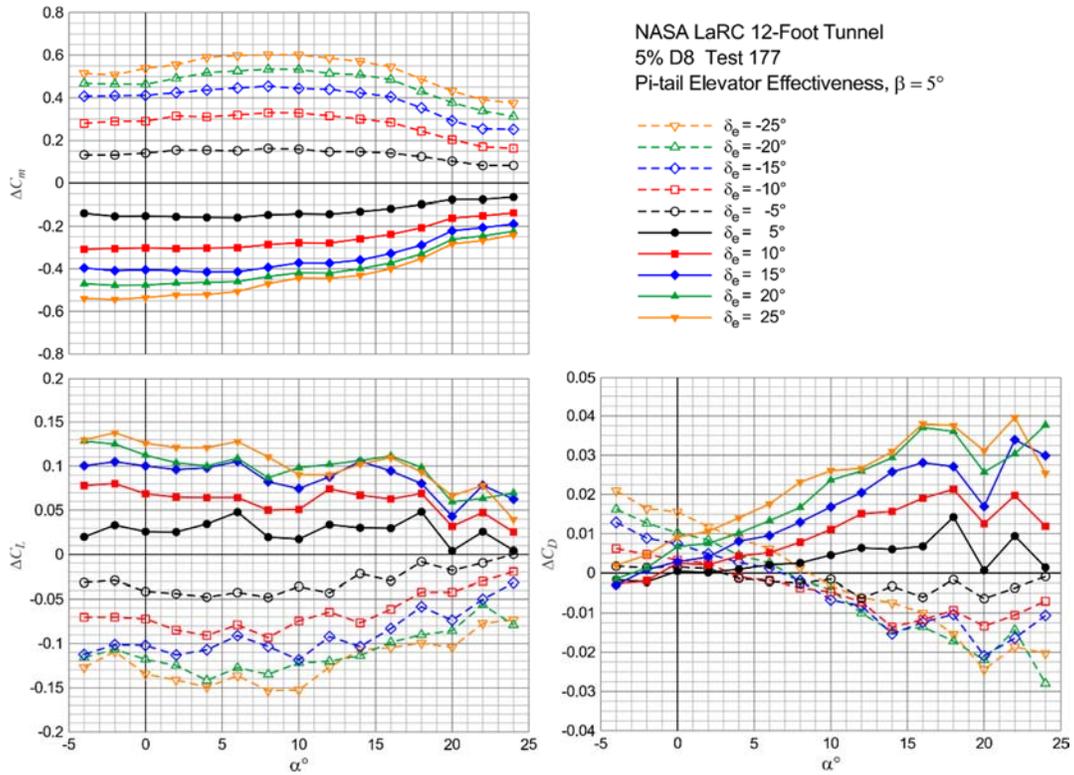
Figure 49 – Pi-tail elevator longitudinal control increments with 5° of sideslip.
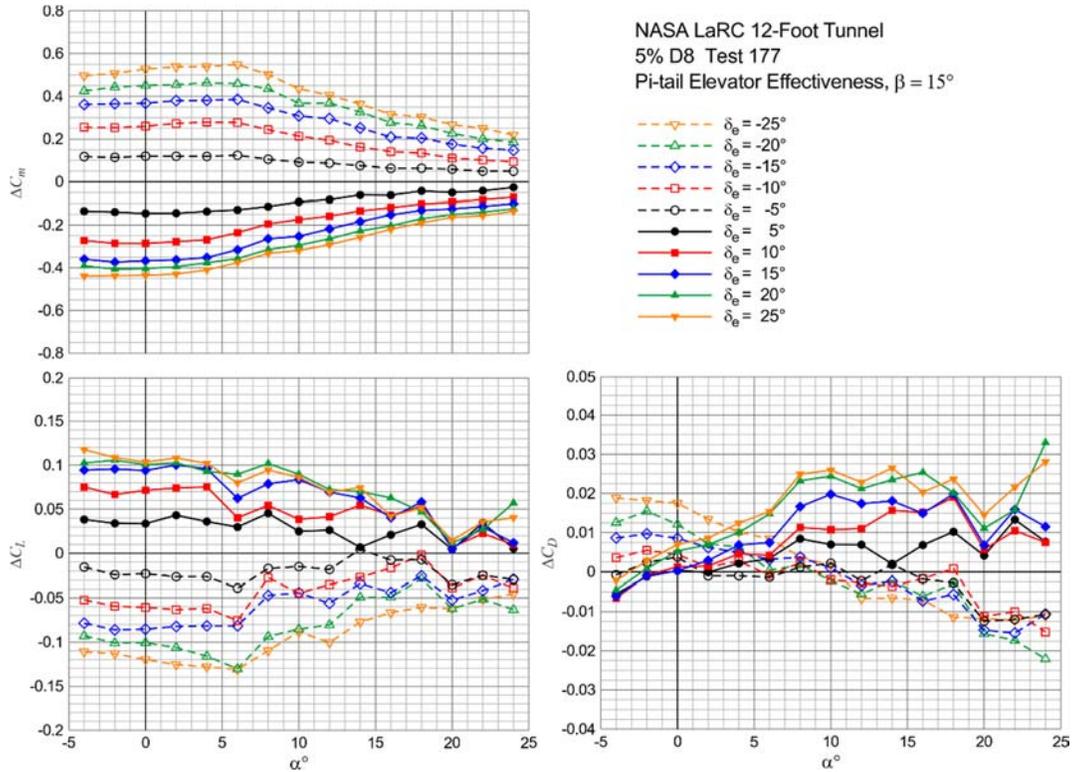
Figure 50 – Pi-tail elevator longitudinal control increments with 15° of sideslip.
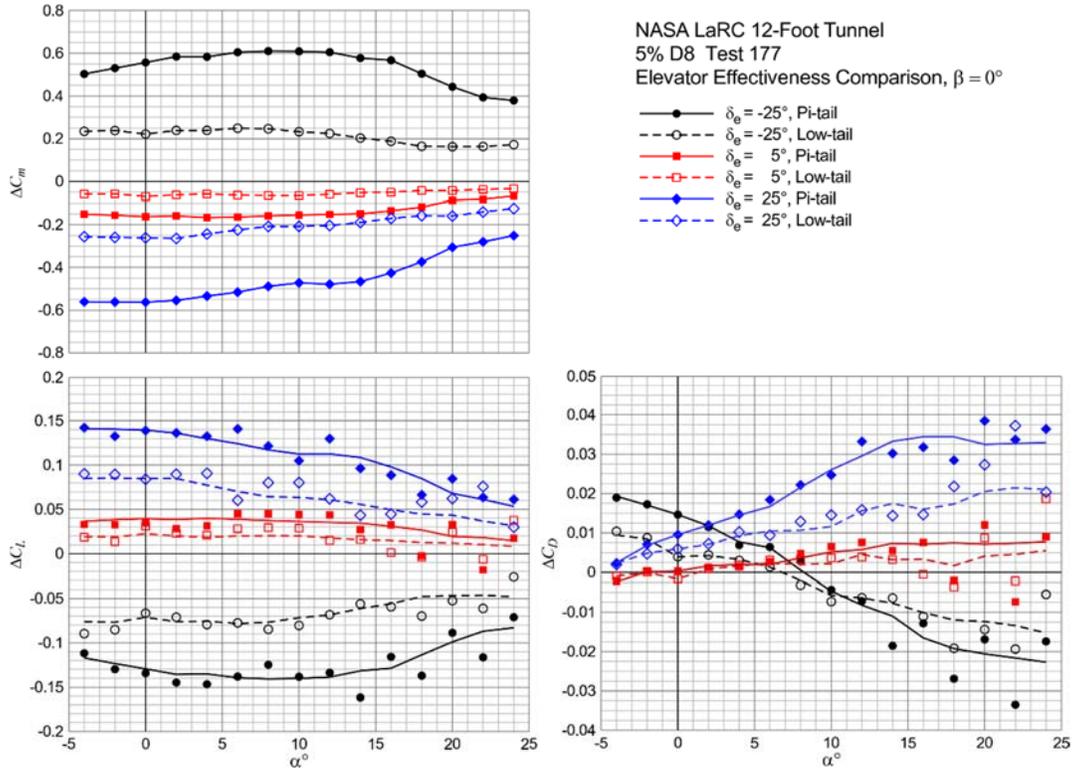
Figure 51 – Pi-tail and Low-tail elevator effectiveness comparison.

Rudder Effectiveness

The Pi-tail rudder lateral/directional control increments multiplied by the sign of the control deflection are shown in figure 52 with angle of attack. The increments are presented in this manner to check for flow or model asymmetry. If the model and flow are symmetric then the positive and negative deflection increments will match. The rolling and yawing moment increments show reasonable agreement. However, the sideforce increments for the ±5° and ±15° deflections show large offsets even though the yawing moments reasonably agree. In an effort to resolve this discrepancy the rudder moment arm was computed in a similar manner as the previously computed stabilizer and elevator moment arms. The rudder nondimensional horizontal moment arm is the negative ratio of the yawing moment and sideforce coefficients

$$\bar{x}_r = -\frac{\Delta C_n}{\Delta C_Y} \qquad (8)$$

Figure 53 shows the rudder moment arm values computed from the control increments presented in figure 52. Also shown on the figure and presented as equation 9 is a linear fit of the moment arm values that lie within the geometric limits of the vertical fin.

$$\bar{x}_r = -0.0011\alpha + 0.3726 \qquad (9)$$

A new set of sideforce increments was computed using the moment arm values of equation 9 and the yawing moment coefficient increments. These new values are presented in figure 54 as lines and dashed lines along with the original measured values shown as symbols. These new moment arm derived values show the -5° and -15° measured sideforce increments to be inconsistent with the other measured and derived results.
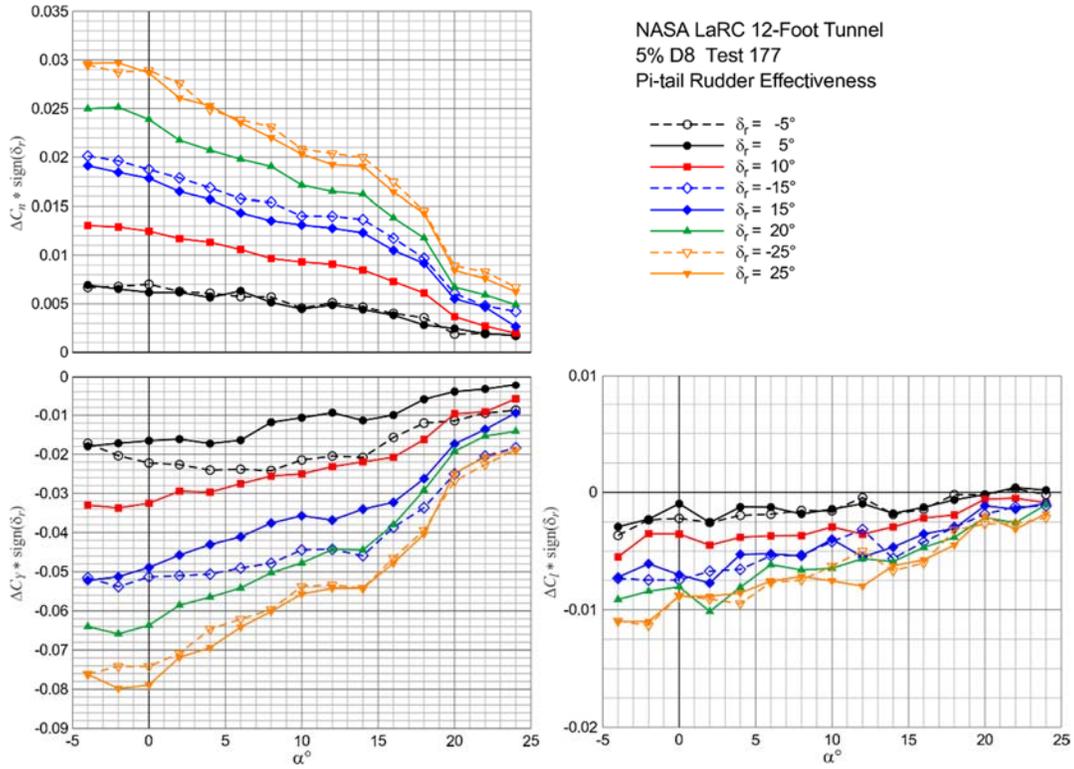

Figure 52 – Pi-tail rudder lateral/directional control increments multiplied by the sign of the control deflection.
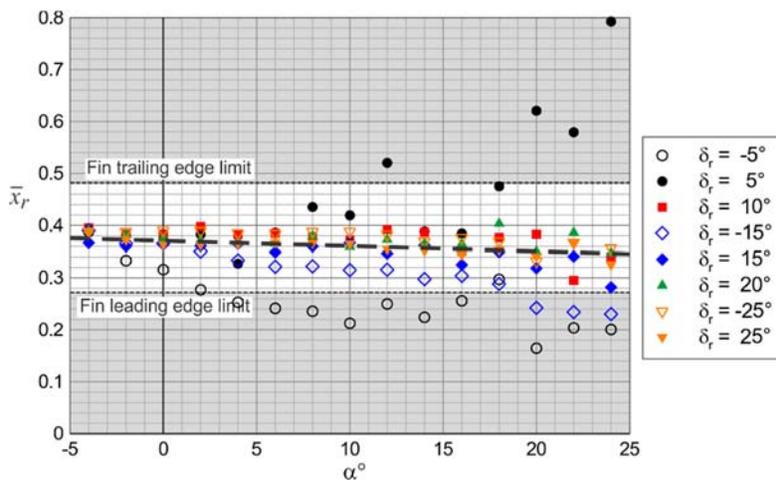

Figure 53 – Linear fit of rudder nondimensional horizontal moment arm derived from Pi-tail control increments.
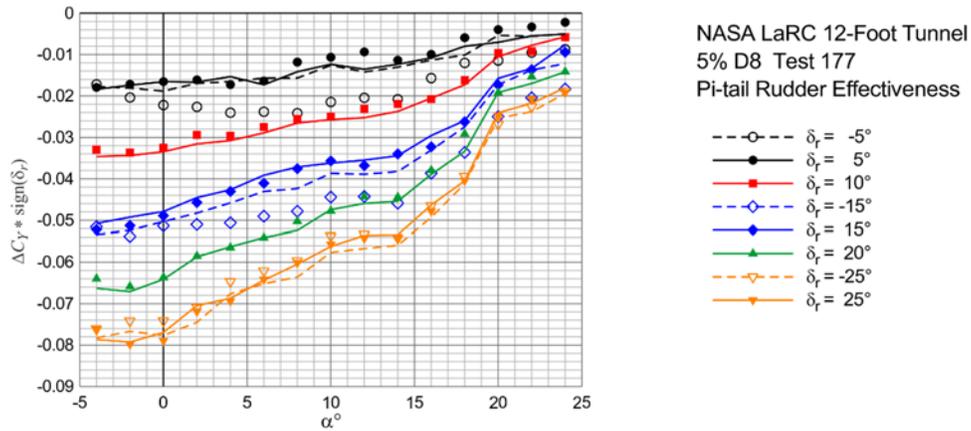
Figure 54 – Pi-tail rudder sideforce increments with moment arm based fit values (lines)

Figure 55 shows the Pi-tail rudder lateral/directional control increments plotted as a function of the magnitude of the rudder deflection at fixed angle of attack values. The negative deflection values are denoted with dashed lines. The rudder control increments are nearly linear with control deflection and the control effectiveness diminishes with increased angle of attack. As noted previously in figure 52, the moment increments for positive and negative deflections are fairly symmetric. The sideforce increments are from the moment arm fit values shown in figure 54.
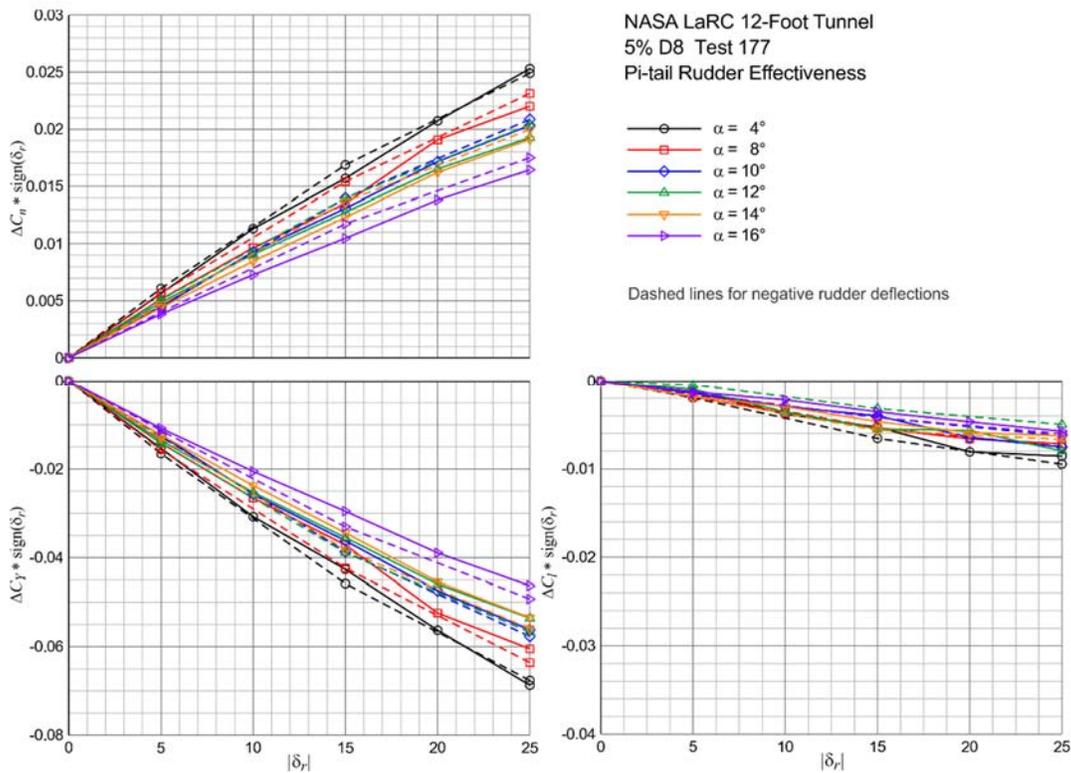

Figure 55 – Pi-tail lateral/directional control increments with rudder deflection at fixed angles of attack.

The vertical fin and rudder planforms of the Low-tail empennage are the same as those for the Pi-tail. The only geometry difference that could impact the rudder control effectiveness is the horizontal stabilizer location. Figure 56 shows the Low-tail rudder lateral/directional control increments multiplied by the sign

39

of the rudder deflection at fixed deflection values with angle of attack. Once again there is a noticeable offset between sideforce increments for the -25° and +25° rudder deflections.
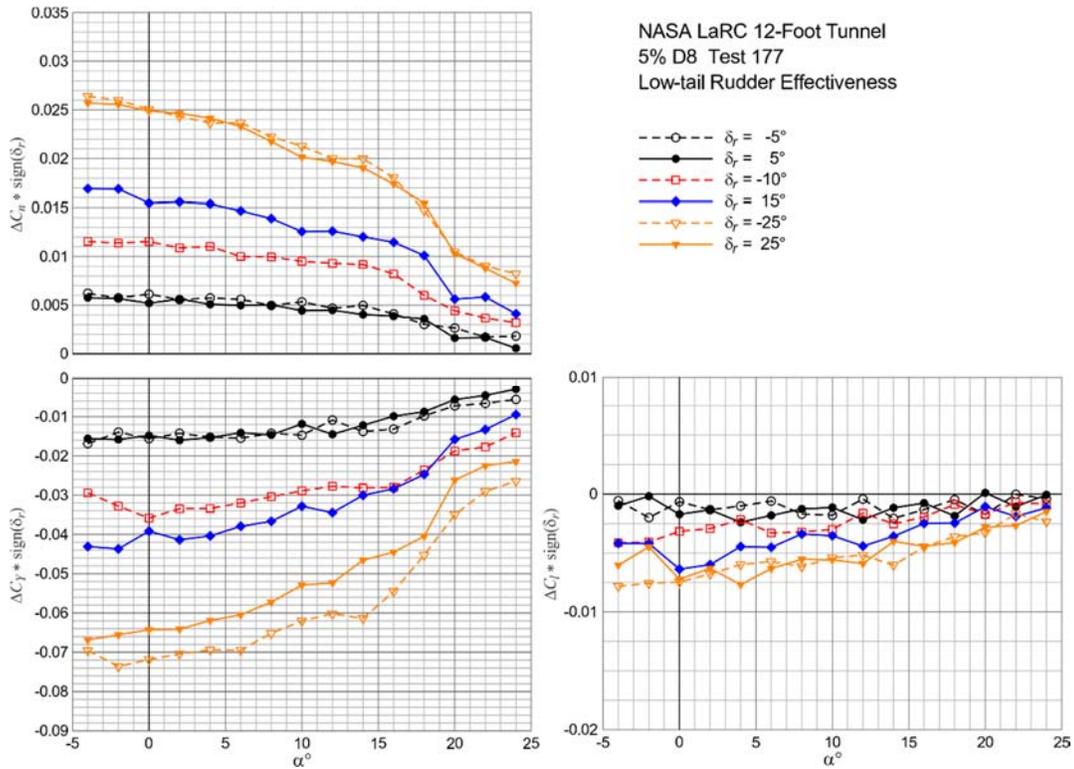

Figure 56 – Low-tail rudder lateral/directional control increments multiplied by the sign of the control deflection.

Figure 57 shows the Low-tail rudder moment arm values computed from the control increments presented in figure 56. Also shown on the figure and presented as equation 10 is a linear fit of the moment arm values that lie within the geometric limits of the vertical fin.

$$\bar{x}_r = -0.0006\alpha + 0.3673 \tag{10}$$
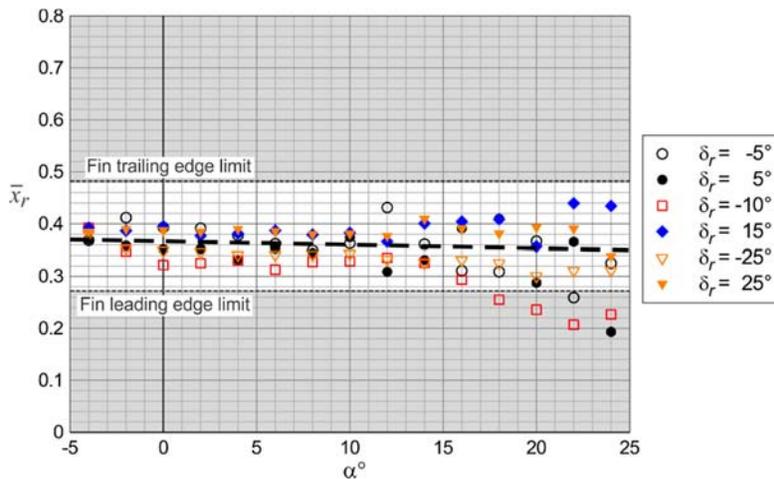
Figure 57 – Linear fit of rudder nondimensional horizontal moment arm derived from Low-tail control increments.

A new set of Low-tail sideforce increments were computed using the moment arm values of equation 10 and the yawing moment coefficient increments. These new values are presented in figure 58 as lines and dashed lines along with the original measured values shown as symbols. These Low-tail moment arm derived values again illustrate the inconsistency of the measured sideforce increments.
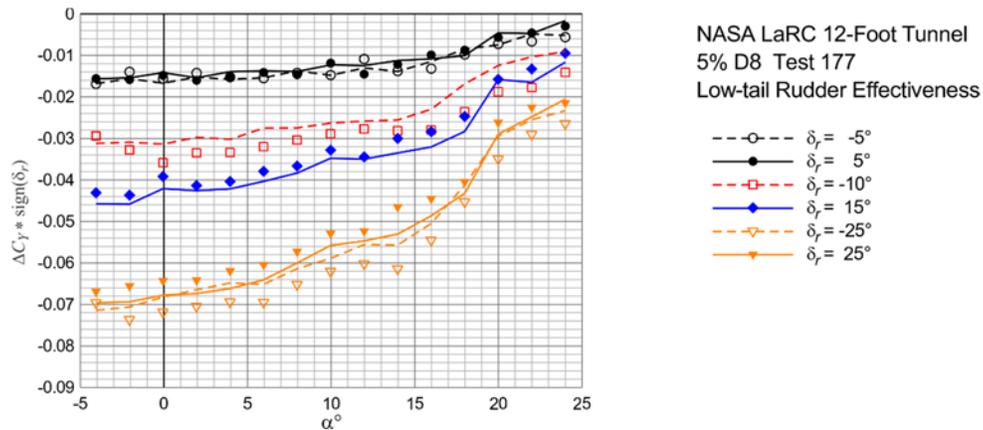

Figure 58 – Low-tail rudder sideforce increments with moment arm based fit values (lines).

Figure 59 shows a comparison of the Pi-tail and Low-tail rudder control increments with angle of attack. The sideforce increments shown are both the measured, denoted with the symbols, and the moment arm fit values, donated with the lines. As previously noted the vertical fin and rudder planforms of the Low-tail empennage are the same as those for the Pi-tail with the only difference being the location of the stabilizer. So it is not surprising that the rudder control increments of the Low-tail and Pi-tail are very similar. The only significant difference being at the lower angles of attack with the higher control deflections where the Pi-tail rudder is a little more effective.
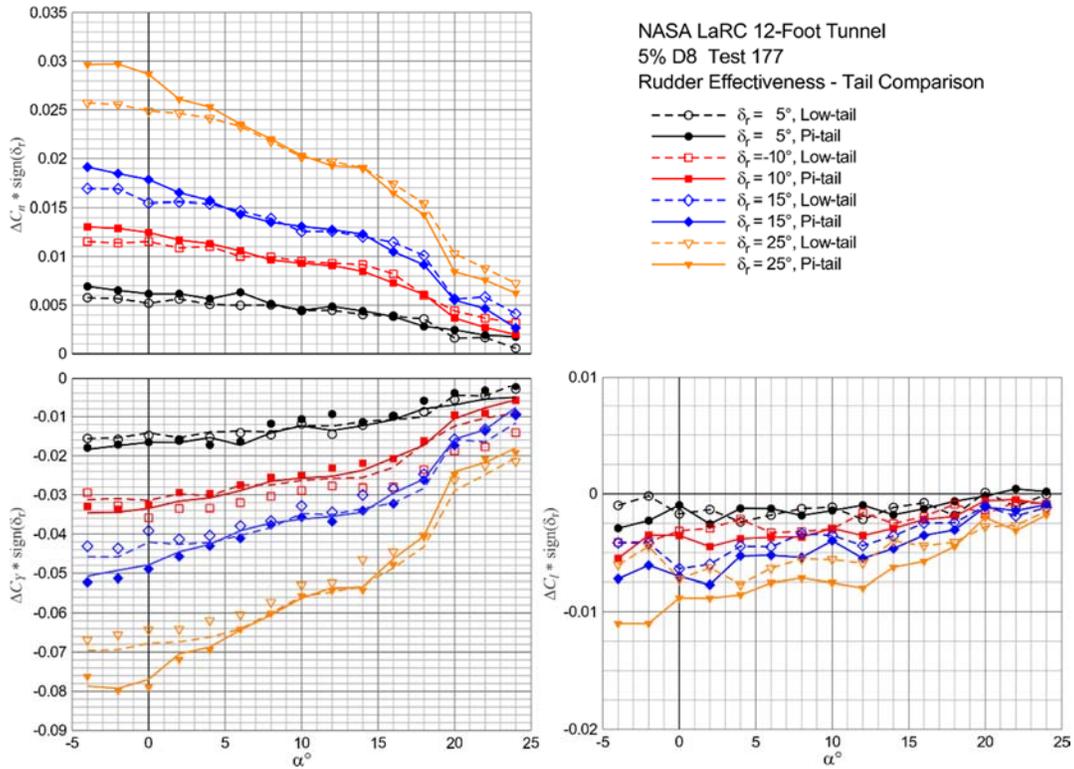
Figure 59 – Comparison of the Pi-tail and Low-tail rudder control increments with angle of attack

The effects of sideslip angle on the rudder control effectiveness are presented in figures 60 and 61 for angles of attack of 8° and 14°, respectively. These figures show the lateral/directional control increments plotted against the sideslip angle multiplied by the sign of the rudder deflection. This method of presentation provides a check of the symmetry of the data. A rudder deflection with negative sideslip should provide the same magnitude of control increment as a rudder deflection in the opposite direction with a positive sideslip angle. The ±5° rudder deflections shown in the figures provide this comparison. The symmetry of moment increments compares well. The effect of the sideslip angle on the rudder effectiveness appears to increase with the magnitude of the rudder deflection and sideslip angle. The control effectiveness appears to peak at 5° sideslip in the opposite direction of rudder deflection ($\beta * \text{sign}(\delta_r) = -5°$). The sideforce increments show similar measurement fluctuations as those previously noted in figures 52 and 56.
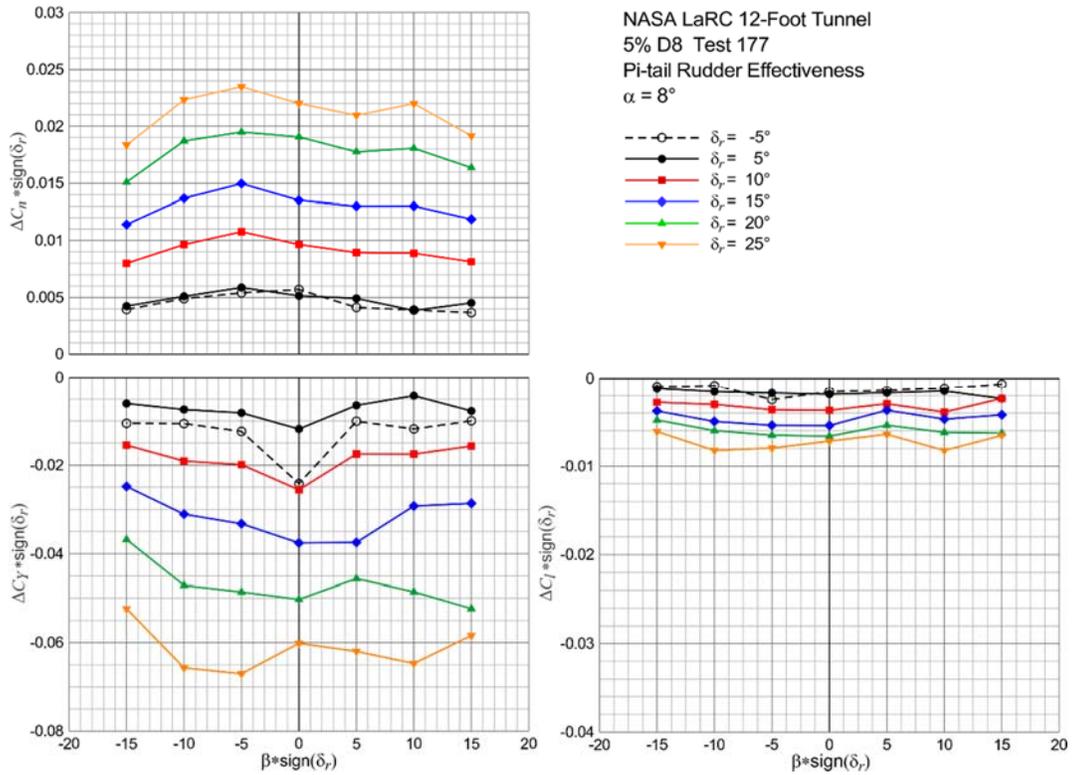
Figure 60 – Effect of sideslip angle on Pi-tail rudder control effectiveness at 8° angle of attack.
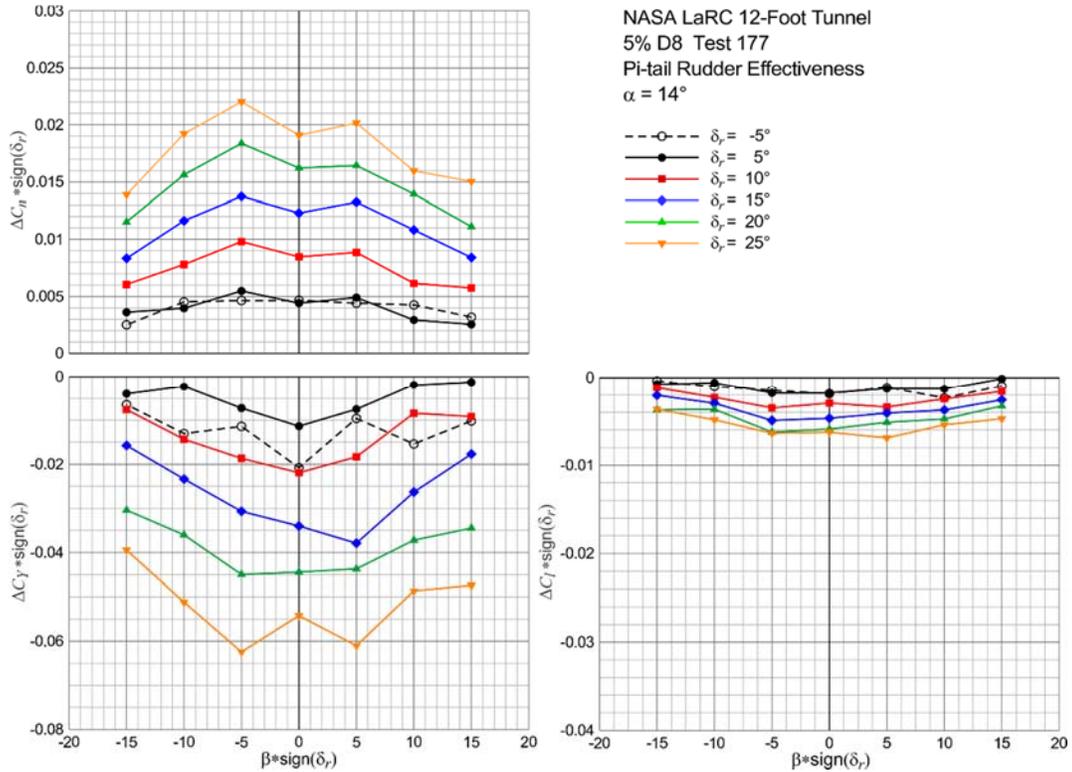
Figure 61 – Effect of sideslip angle on Pi-tail rudder control effectiveness at 14° angle of attack

The aft sweep of the rudder hinge line provides the opportunity for the rudders to provide a longitudinal control increment when deflected asymmetrically. The magnitude of this longitudinal increment was measured with both rudders deflected 25° inboard and both deflected 25° outboard, as shown in figure 62. The resultant longitudinal control increments for both the Pi-tail and Low-tail are presented in figure 63. A small pitch increment is obtained with the asymmetric rudder deflections but it is less than that achieved with 5° of elevator deflection.
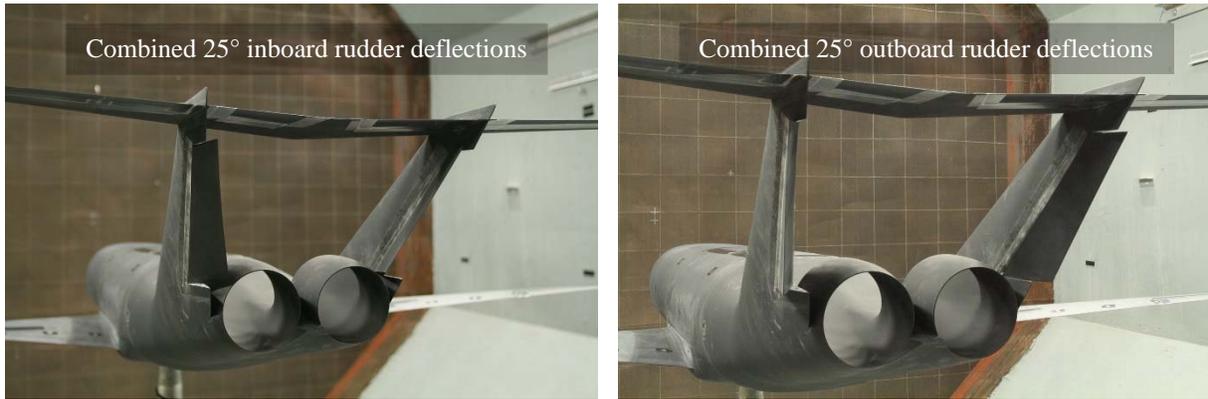
Figure 62 – Pictures of combined 25° inboard and outboard rudder deflections.
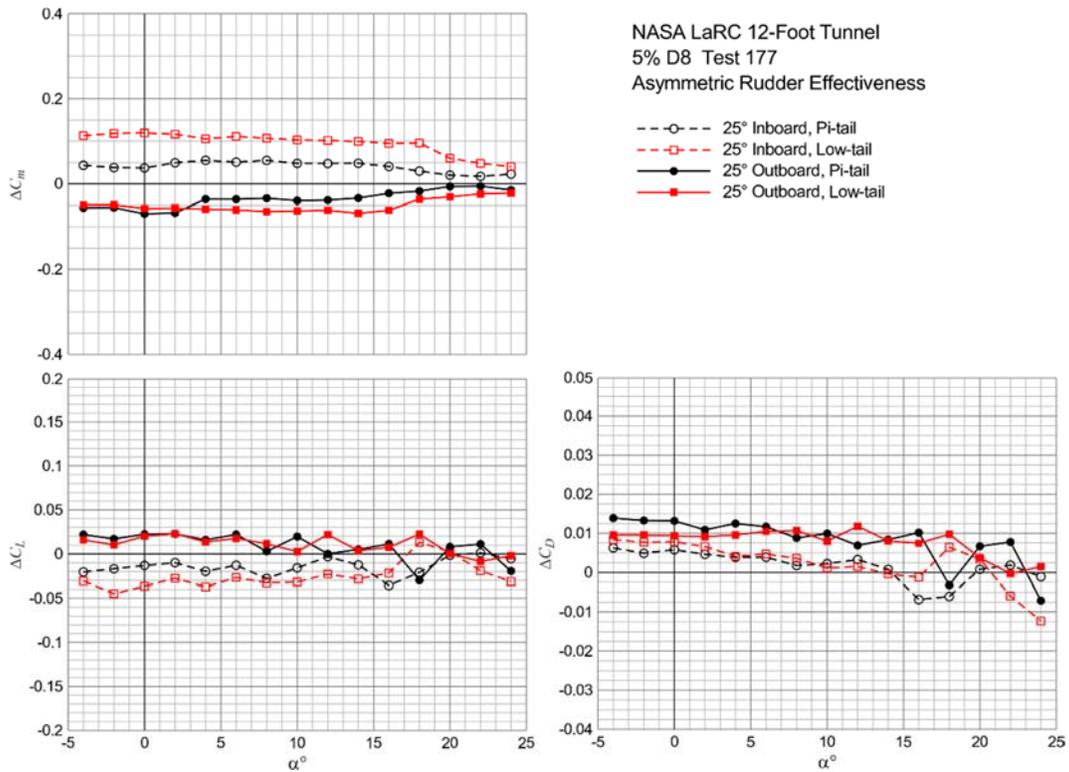
Figure 63 – Longitudinal effect of asymmetric rudder deflections.

Aileron Effectiveness

The effects of left aileron control deflections on the rolling moment increments at zero sideslip are shown in figure 64. The aileron roll control effectiveness declines slightly with increased angle of attack. The effects of deflection angle on the left aileron rolling moment increments at fixed angles of attack are shown in figure 65. The roll control effectiveness begins to diminish at positive control deflections greater than 10°.
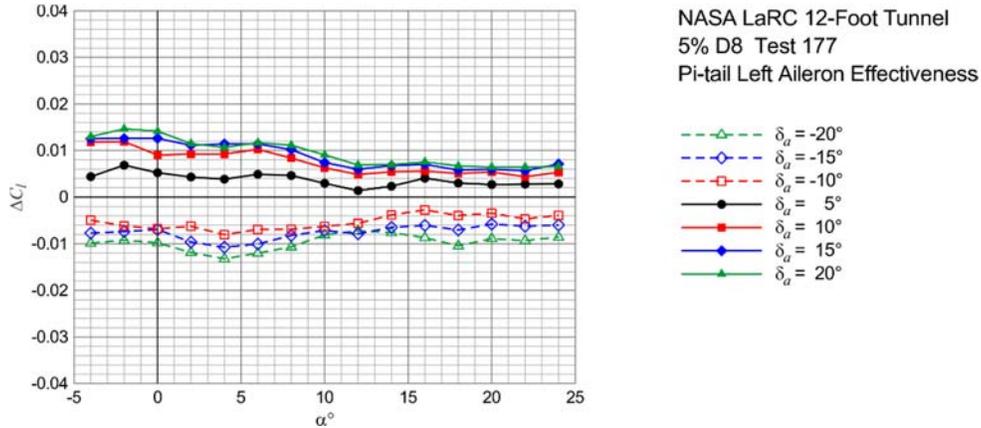

Figure 64 – Left aileron rolling moment increments with angle of attack.
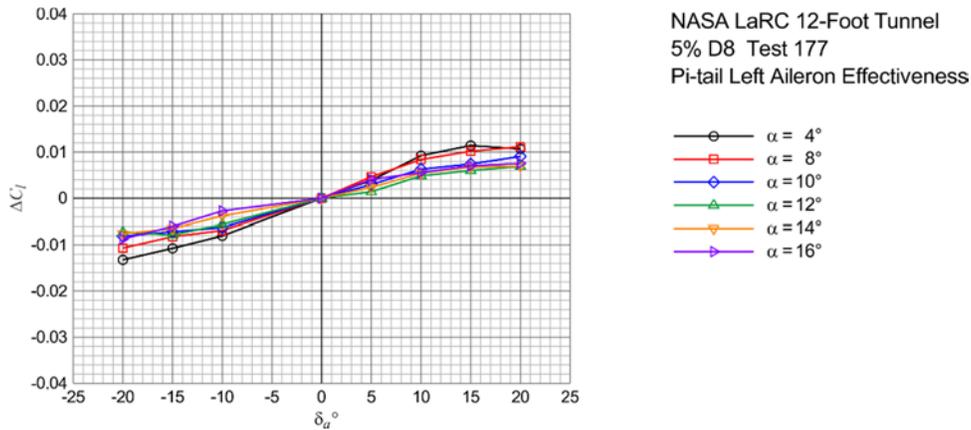
Figure 65 – Effect of left aileron deflection angle on rolling moment increments at fixed angles of attack.

The effects of sideslip angle on the aileron rolling moment increments are presented in figure 66 at a fixed angle of attack of 8°, which is near the end of the configuration linear lift curve. The sideslip effects are not large and appear more pronounced with the negative control deflection (trailing edge up).
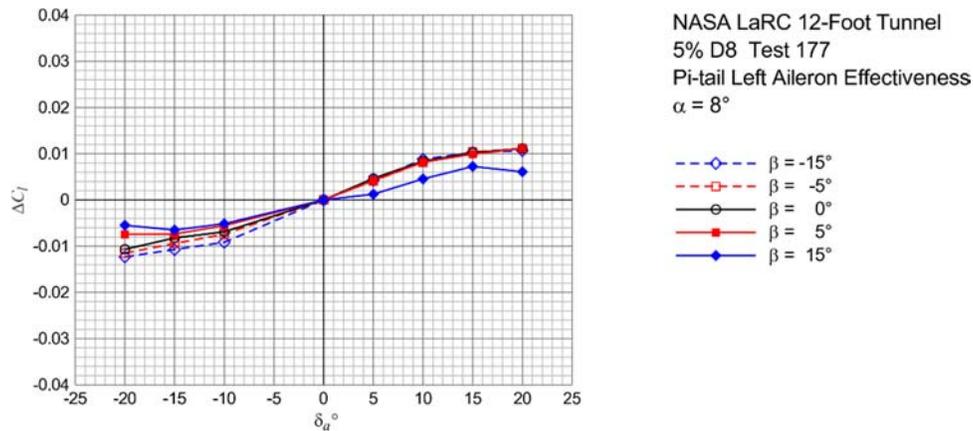
Figure 66 –Effect of sideslip angle on left aileron roll control effectiveness at 8° angle of attack

Summary

A low-speed stability and control test was conducted in the NASA Langley 12-Foot Low-Speed Tunnel on a 5-percent scale model of a "double-bubble" or D8 transport configuration. The test explored the longitudinal and later/directional control characteristics of the configuration as well as investigating the aerodynamic effects of nose and empennage configuration changes.

A few key findings of the test were:

- The baseline nose shape produces a 0.03 pitching moment increase (nose-up) over the conventional nose shape without any measurable difference in lift or drag. This provides a cruise trim increment without elevator or stabilizer defection.

- The Pi-tail provides better pitch stability than the Low-tail. The Low-tail and Pi-tail have the same stabilizer span but the Pi-tail has 1.7 times more horizontal surface area and 1.4 times longer moment arm.

- The vertical fins of the Low-tail configuration appear to have slightly more lateral/directional effectiveness than those of the Pi-tail even though both have identical planforms. The capping of the vertical fins with the Pi-tail stabilizer may have reduced the vertical fin efficiency.

The variation in data repeatability was greater than the balance resolution for all the forces and moments except the axial force component. That being said, this is still a useful dataset for simulation model development. The deflected control surface normal and sideforce increments showed large variations relative to the moment increments. A method of computing alternate force increments using the control moment increments and a fit of the effective moment arm provided useful results.

References

1 Greitzer, E.M.; et al.: *"N+3 Aircraft Concept Designs and Trade Studies, Final Report,"* Vol. 1 and 2, NASA/CR-2010-216794, Dec. 2010.

2 Drela, M.: "Development of the D8 Transport Configuration," *29th AIAA Applied Aerodynamics Conference,* Honolulu, HI, 27-30 June 2011, AIAA 2011-3970.

3 Pandya, S.: "External Aerodynamics Simulations for the MIT D8 "Double-Bubble" Aircraft Design," *7th International Conference on computational Fluid Dynamics*, Big Island, HI, 9-13 July 2012, ICCFD7-4304.

4 Uranga, A.; Drela, M.; Greitzer, E.; Titchener, N.; Lieu, M.; Siu, N.; Huang, A.; Gatlin, G.; and Hannon, J.: "Preliminary Experimental Assessment of the Boundary Layer Ingestion Benefit for the D8 Aircraft," *52nd AIAA Aerospace Sciences Meeting*, National Harbor, MD, 13-17 January 2014, AIAA 2014-0906.

5 Pandya, S.; Huang, A.; Espitia, A.; and Uranga, A.: "Computational Assessment of the Boundary Layer Ingesting Nacelle Design of the D8 Aircraft," *52nd AIAA Aerospace Sciences Meeting*, National Harbor, MD, 13-17 January 2014, AIAA 2014-0907.

6 Lord, W.; Suciu, G.; Hasel, K.; and Chandler, J.: "Engine Architecture for High Efficiency at Small Core Size," *53rd AIAA Aerospace Sciences Meeting*, Kissimmee, FL, 5-9 January 2015, AIAA 2015-0071.

7 Sabo, K.; and Drela, M.: "Benefits of Boundary Layer Ingestion Propulsion," *53rd AIAA Aerospace Sciences Meeting*, Kissimmee, FL, 5-9 January 2015, AIAA 2015-1667.

8 Shortal, J.; and Osterhout, C.: "*Preliminary Stability and Control Tests in the NACA Free-Flight Wind Tunnel and Correlation with Full-Scale Flight Tests*," NACA TN 810, June 1941.

9 Langley GIS Team: *"12-Foot Low Speed Tunnel"*, last modified on July 26 2016, https://crgis.ndc.nasa.gov/historic/12-Foot_Low_Speed_Tunnel, Accessed October 14, 2016.

REPORT DOCUMENTATION PAGE

1. REPORT DATE *(DD-MM-YYYY)*	2. REPORT TYPE	3. DATES COVERED *(From - To)*
1-12-2017	Technical Memorandum	

4. TITLE AND SUBTITLE	5a. CONTRACT NUMBER
Low-Speed Stability and Control Test of a "Double-Bubble" Transport Configuration	
	5b. GRANT NUMBER
	5c. PROGRAM ELEMENT NUMBER
6. AUTHOR(S)	5d. PROJECT NUMBER
Vicroy, Dan D.	
	5e. TASK NUMBER
	5f. WORK UNIT NUMBER
	107210.02.02.07

7. PERFORMING ORGANIZATION NAME(S) AND ADDRESS(ES)	8. PERFORMING ORGANIZATION REPORT NUMBER
NASA Langley Research Center Hampton, VA 23681-2199	L-20897

9. SPONSORING/MONITORING AGENCY NAME(S) AND ADDRESS(ES)	10. SPONSOR/MONITOR'S ACRONYM(S)
National Aeronautics and Space Administration Washington, DC 20546-0001	NASA
	11. SPONSOR/MONITOR'S REPORT NUMBER(S)
	NASA-TM-2017-219797

12. DISTRIBUTION/AVAILABILITY STATEMENT

Unclassified
Subject Category 08
Availability: NASA STI Program (757) 864-9658

13. SUPPLEMENTARY NOTES

14. ABSTRACT

A test in the Langley 12-Foot Low-Speed Tunnel was conducted as a risk mitigation effort to quickly obtain some low-speed stability and control data on a "double-bubble" or D8 transport configuration. The test also tested some configuration design trades. A 5-percent scale model was tested with stabilizer, elevator, rudder and aileron control deflections. This report summarizes the test results.

15. SUBJECT TERMS

D8; Double-Bubble; Stability and Control; Wind Tunnel Test

16. SECURITY CLASSIFICATION OF:			17. LIMITATION OF ABSTRACT	18. NUMBER OF PAGES	19a. NAME OF RESPONSIBLE PERSON
a. REPORT	b. ABSTRACT	c. THIS PAGE			STI Help Desk (email: help@sti.nasa.gov)
U	U	U	UU	52	**19b. TELEPHONE NUMBER** *(Include area code)* (757) 864-9658